



# One-step low-temperature synthesis of 0D CeO<sub>2</sub> quantum dots/2D BiOX (X = Cl, Br) nanoplates heterojunctions for highly boosting photo-oxidation and reduction ability

Jian Yang<sup>a,b</sup>, Yujun Liang<sup>a,b,\*</sup>, Kai Li<sup>a,b</sup>, Gui Yang<sup>a,b</sup>, Shu Yin<sup>c,\*\*</sup>

<sup>a</sup> Engineering Research Center of Nano-Geomaterials of Ministry of Education, China University of Geosciences, Wuhan, 430074, China

<sup>b</sup> Faculty of Materials Science and Chemistry, China University of Geosciences, Wuhan, 430074, China

<sup>c</sup> Institute of Multidisciplinary Research for Advanced Materials, Tohoku University, 2-1-1, Katahira, Aoba-ku, Sendai 980-8577, Japan

## ARTICLE INFO

### Keywords:

CeO<sub>2</sub> QDs/BiOX nanoplates

Ce<sup>4+</sup>/Ce<sup>3+</sup> redox centers

Photo-oxidation

Photo-reduction

## ABSTRACT

0D/2D heterojunctions, especially quantum dots (QDs)/nanoplates have attracted noteworthy attention for use of the high charge mobility of photoinduced electrons and holes. Herein, we report a novel one-step low-temperature route for the controlled synthesis of CeO<sub>2</sub> QDs/BiOX (X = Cl, Br) nanoplates heterojunctions with the self-created in-built Ce<sup>4+</sup>/Ce<sup>3+</sup> redox centers. The as-prepared heterojunctions exhibited outstanding photocatalytic abilities not only for the oxidation of tetracycline (TC) but also for the reduction of hexavalent chromium (Cr<sup>6+</sup>) although under 5 W white LED light irradiation. The considerably enhanced capabilities were attributed to the improvement of light absorption and the highly effective transfer and separation of photo-excited carriers, which encouraged by the strong synergistic effects of inner Ce<sup>4+</sup>/Ce<sup>3+</sup> redox centers and the formation of intimately contacted interface between CeO<sub>2</sub> QDs and BiOX nanoplates. Meanwhile, the likely degradation pathway of TC was proposed on the basis of the intermediate products detected by GC-MS, and the appearance photocatalytic mechanisms were also discussed in detail. This work could open new possibilities to provide some insight into a facile, energy saving and environmental friendly pathway for synthesizing versatile 0D/2D Bi-based heterojunction materials with high photocatalytic performance.

## 1. Introduction

Bismuth oxyhalide, BiOX (X = Cl, Br), have been considered as one of the most promising class of catalysts with excellent photocatalytic performance, attributing to the structural characteristic that the layered structure in the [001] direction could provide an internal static electric fields to afford a potential driving force for the separation of photo-generated carriers [1–3]. Nevertheless, the commercialization and practical functional application of BiOX (X = Cl, Br) are still constrained by some key scientific problems, which include the low quantum efficiency of individual materials, poor utilization of solar energy, and slow rate of charge transfer [4,5]. By considering a much related topic, the construction of heterojunctions have been proposed and developed to be one of the most forward-looking means to harvest energy from the visible-light region and improve the visible light photocatalytic activity of BiOX (X = Cl, Br), such as g-C<sub>3</sub>N<sub>4</sub>/BiOCl [6], TiO<sub>2</sub>/BiOBr [7], Ag/AgX/BiOX [8] and so on.

As a nontoxic and inexpensive rare earth material, cubic fluorite cerium dioxide (CeO<sub>2</sub>) could be served as an ideal photocatalyst owing to its high stability, narrow band gap and promising photocatalytic efficiency for the degradation of various pollutants and water-splitting for H<sub>2</sub> production [9]. These unique merits make it become a promising candidate to modify the BiOX (X = Cl, Br) for improving their visible light activity. Under this consideration, there were some reports on the two steps synthesis of CeO<sub>2</sub>/BiOCl and CeO<sub>2</sub>/BiOBr heterostructures with excellent photocatalytic performance [10–12]. However, it was still some space for further enhancing the photocatalytic performance via optimizing the morphology, synthesis methods, and coupling tightness of CeO<sub>2</sub> and BiOX (X = Cl, Br). For decades, 0 dimensional (0D) semiconductor quantum dots (QDs) have attracted significant attention and widely used extensively in the field of photocatalysts, photovoltaic devices, photodetectors and phototransistors [13,14]. In fact, CeO<sub>2</sub> QDs might display favorable photocatalytic activity because the small-size effect and higher quantum confinement could afford

\* Corresponding author at: Engineering Research Center of Nano-Geomaterials of Ministry of Education, China University of Geosciences, Wuhan, 430074, China.

\*\* Corresponding author.

E-mail addresses: [yujunliang@sohu.com](mailto:yujunliang@sohu.com) (Y. Liang), [shuyin@tagen.tohoku.ac.jp](mailto:shuyin@tagen.tohoku.ac.jp) (S. Yin).

<https://doi.org/10.1016/j.apcatb.2019.03.017>

Received 13 November 2018; Received in revised form 21 February 2019; Accepted 6 March 2019

Available online 07 March 2019

0926-3373/© 2019 Elsevier B.V. All rights reserved.

more opportunity to connect with other atoms in a heterostructure system, resulting in a more closely contacted interface between two components [15]. Moreover, the shorter average diffusion time from bulk to surface could also reduce the charge carrier recombination [16]. Despite these promises, like other semiconductor QDs, the photocatalytic performance of  $\text{CeO}_2$  QDs was significantly limited by its intrinsic drawbacks of self-aggregation and abundant surface defects, which made them unstable compared with the bulk ones [14]. In this regard, we hypothesized that loading  $\text{CeO}_2$  QDs onto 2D BiOX ( $X = \text{Cl}, \text{Br}$ ) to form a 0D/2D heterojunction system would be a favorable choice to make  $\text{CeO}_2$  QDs more dispersive and stable, while the enhanced charge transfer could also be successfully realized. To the best of our knowledge, few relative articles about 0D  $\text{CeO}_2$  QDs or  $\text{CeO}_2$  QDs-based photocatalysts have been reported. Meanwhile, in theory, BiOX ( $X = \text{Cl}, \text{Br}$ ) have a tendency to grow into nanosheets/plates with 2D features owing to their highly anisotropic layered structures [3]. Accordingly, the fabrication of 0D  $\text{CeO}_2$ /2D BiOX ( $X = \text{Cl}, \text{Br}$ ) intimate contact heterojunctions with superior photocatalytic activity is highly desirable and anticipated.

Generally, the traditional synthesis methods of heterojunction materials mainly include chemical precipitation, electrodeposition, hydrothermal, ion exchange and vapor deposition etc. [17–24]. However, these conventional preparation approaches still have such limitations as high pressure conditions, complicated manipulation, and specific requirement of equipment and/or large consumption of organic agents. Consequently, it is highly desirable to develop a facile, environmental friendly and low-temperature route to prepare 0D  $\text{CeO}_2$ /2D BiOX ( $X = \text{Cl}, \text{Br}$ ) heterostructures. Aware of that the melting points of  $\text{Bi}(\text{NO}_3)_3 \cdot 5\text{H}_2\text{O}$  and  $\text{Ce}(\text{NO}_3)_3 \cdot 6\text{H}_2\text{O}$  are relative low, so their mixture would be easily to form a molten state after reaching a particular temperature, which the molten salt medium could offer a suitable reaction condition with a high ion concentration and accelerate the diffusion speeds of reacting constituents. Therefore, it might be a fantasy one-pot method to construct 0D  $\text{CeO}_2$ /2D BiOX ( $X = \text{Cl}, \text{Br}$ ) heterojunctions via calcining the mixture of  $\text{Ce}(\text{NO}_3)_3 \cdot 6\text{H}_2\text{O}$ ,  $\text{Bi}(\text{NO}_3)_3 \cdot 5\text{H}_2\text{O}$  and  $\text{NaCl}/\text{NaBr}$ .

On the basis of the above concepts and ideas, herein, we developed a facile and low-temperature approach for the preparation of visible light driven  $\text{CeO}_2$  QDs/BiOX ( $X = \text{Cl}, \text{Br}$ ) nanoplates heterostructures. We interestingly found that the in-built  $\text{Ce}^{4+}/\text{Ce}^{3+}$  redox centers were created while the formation of intimately contacted interface between  $\text{CeO}_2$  QDs and BiOX ( $X = \text{Cl}, \text{Br}$ ). The photocatalytic performances of the as-prepared samples were investigated via the oxidation of tetracycline (TC), RhB and the reduction of  $\text{Cr}^{6+}$  under 5 W white LED light irradiation, which are typical antibiotics, organic dyes and heavy metal contaminants in the wastewater. It was found that the  $\text{CeO}_2$  QDs/BiOX ( $X = \text{Cl}, \text{Br}$ ) heterojunctions displayed more remarkable photocatalytic oxidation and reduction ability than that of pristine BiOCl, BiOBr and  $\text{CeO}_2$ , respectively. Furthermore, the comprehensive photocatalytic mechanisms of  $\text{CeO}_2$ /BiOCl and  $\text{CeO}_2$ /BiOBr heterostructures were also proposed and discussed in detail respectively.

## 2. Experimental section

### 2.1. Synthesis of BiOX nanoplates and $\text{CeO}_2$ QDs/BiOX ( $X = \text{Cl}, \text{Br}$ ) heterostructures

The chemicals used in this work were of analytical reagent grade and without further purification. The BiOX nanoplates and  $\text{CeO}_2$  QDs/BiOX ( $X = \text{Cl}, \text{Br}$ ) heterostructures with the  $\text{Ce}^{4+}/\text{Ce}^{3+}$  redox centers were synthesized by a simplistic one-step low-temperature synthesis method, and the general process is illustrated in Fig. 1. Different contents of  $\text{CeO}_2$  in the  $\text{CeO}_2$ /BiOX ( $X = \text{Cl}, \text{Br}$ ) heterojunctions were achieved by adjusting the Ce/Bi molar ratio of the raw materials. In a typical process,  $\text{Bi}(\text{NO}_3)_3 \cdot 5\text{H}_2\text{O}$  (2 mmol),  $\text{NaCl}/\text{NaBr}$  (2 mmol) and  $\text{Ce}(\text{NO}_3)_3 \cdot 6\text{H}_2\text{O}$  with appropriate stoichiometric amounts were mixed in

logical order and grinded thoroughly for over 20 min in an agate mortar. After that, the grinded mixture were placed in an alumina crucible and calcined at 300 °C for 4 h, while the heating rate was 2 °C/min. The reaction system is in a molten state at 300 °C. Finally, the obtained samples were washed with hot deionized water and ethanol for several times, and then dried at 80 °C overnight. The  $\text{CeO}_2$ /BiOX ( $X = \text{Cl}, \text{Br}$ ) composite photocatalysts with different amounts of  $\text{CeO}_2$  which were 1 mol%, 5 mol%, 10 mol%, and 20 mol%. In general, we denoted the as-prepared  $\text{CeO}_2$ /BiOCl samples as 0.01CBC, 0.05CBC, 0.10CBC and 0.20CBC, respectively. Similarly, the as-prepared  $\text{CeO}_2$ /BiOBr samples were denoted as 0.01CBB, 0.05CBB, 0.10CBB and 0.20CBB, respectively. For comparison, the pure  $\text{CeO}_2$  was also obtained under the same conditions in the absence of  $\text{Bi}(\text{NO}_3)_3 \cdot 5\text{H}_2\text{O}$  and  $\text{NaCl}/\text{NaBr}$ .

### 2.2. Characterization

The phase composition of the as-prepared samples was investigated using X-ray powder diffraction on an X-ray diffractometer (D8-FOCUS, Bruker, Germany) using  $\text{Cu K}\alpha$  radiation ( $\lambda = 1.5418 \text{ \AA}$ ). The morphology and microstructure were examined by field emission scanning electron microscope (FE-SEM, SU8010, Hitachi, Japan), transmission electron microscopy (TEM, Tecnai G2 T20, FEI, America) and high-resolution TEM (HRTEM). Meanwhile, the chemical compositions and mapping images of the products were employed by the energy dispersive spectrum (EDS) which was attached to the SEM. To analyze the chemical states and surface composition of samples, the X-ray photoelectron spectroscopy (XPS) measurement was done on a Thermo Scientific Escalab 250X spectrometer using 150 W Al  $\text{K}\alpha$  X-ray sources, and all the binding energies were referenced to the  $\text{C} 1s$  peak at 284.6 eV of the surface adventitious carbon. UV–vis diffuse reflectance spectra (DRS) were recorded on an UV-2550PC spectrophotometer (Shimadzu Corporation, Japan) equipped with a 150 W xenon lamp as the excitation source, using  $\text{BaSO}_4$  as a reference. The total organic carbon (TOC) analyses were conducted on a TOC-VCPN analyzer. The photoluminescence emission spectra of photocatalysts were performed with a fluorescence spectrometer (Fluoromax-4 P, HoribaJobin Yvon, New Jersey, USA), which was equipped with a 150 W xenon lamp as the excitation source. The photoluminescence decay curves were acquired from a Lecroy Wave Runner 18 6100 Digital Oscilloscope (1 GHz) using a tunable laser (pulse width = 4 ns, gate = 5019 ns) as the excitation (Continuum Sunlite OPO).

### 2.3. Photocatalytic activities test

The photocatalytic performances of the as-prepared photocatalysts were systematically evaluated via the photocatalytic degradation of TC, RhB and the reduction of  $\text{Cr}^{6+}$  under visible light irradiation, which are typical antibiotics, organic dyes and heavy metal contaminants in the wastewater. The photocatalysis experiments were conducted in a multipath photochemical reaction system (PCX50B, Beijing Perfect Light Technology co., LTD) which equipped with white 5 W white LEDs as a visible light source, and the spectral range of LED light is displayed in the supporting information (Fig. S1). In detail, 50 mg of the samples was added into 50 mL of TC (10 mg/L), RhB (10 mg/L) or  $\text{Cr}(\text{VI})$  (20 mg/L, which was based on Cr in a dilute  $\text{K}_2\text{Cr}_2\text{O}_7$  solution with citric acid as hole scavenger) solutions, respectively. Prior to irradiation, the suspensions were magnetically stirred for 30 min to reach the adsorption-desorption equilibrium in the dark. Subsequently, the suspension was exposed to visible light. At given time intervals, 4 mL of the aliquots were extracted and centrifuged at 8000 rpm for 2 min to remove the photocatalysts. The filtrates of RhB and TC were subsequently analyzed on UV–vis spectrophotometer at their maximum absorption wavelength, and the concentration of  $\text{Cr}(\text{VI})$  was obtained by a diphenylcarbazide colorimetric method using UV–vis spectroscopy at 540 nm

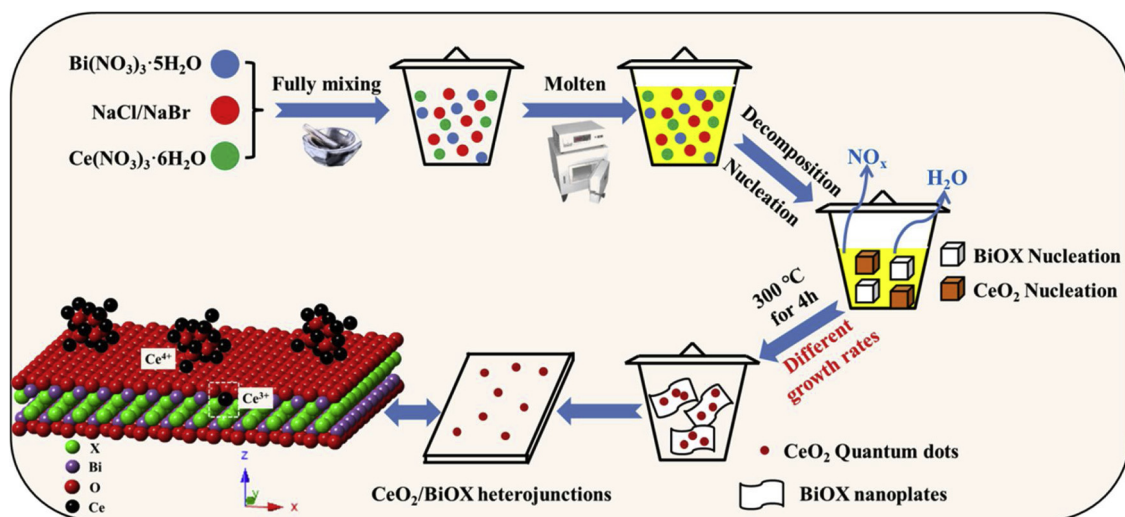


Fig. 1. Schematic illustration of the fabrication of  $\text{CeO}_2$  QDs/ $\text{BiOX}$  ( $X = \text{Cl}, \text{Br}$ ) heterostructures.

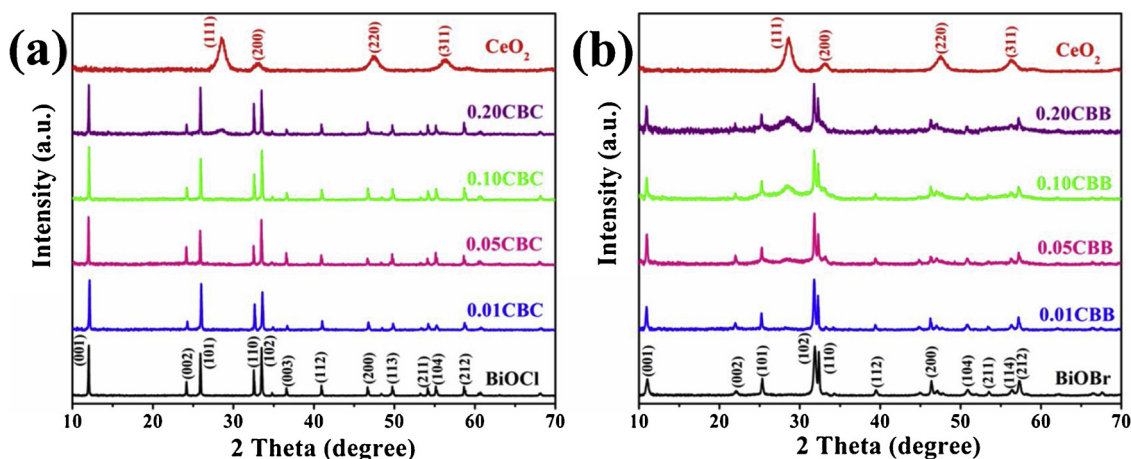
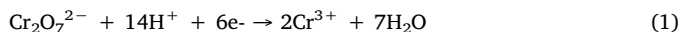


Fig. 2. XRD patterns of (a)  $\text{CeO}_2$ ,  $\text{BiOCl}$  and CBC, (b)  $\text{CeO}_2$ ,  $\text{BiOBr}$  and CBB with different  $\text{CeO}_2$  QDs loading amount.

wavelength.

The intermediates of TC degradation were monitored using a GC–MS system. For the pre-treatment, the degradation solution was adjusted to  $\text{pH} = 2.5$  with 10% HCl. Then, the solution was extracted with 60 mL dichloromethane for three times and concentrated to 1.0 mL by rotary evaporation before analyzed. The column temperature was programmed at  $50^\circ\text{C}$  (hold for 3 min) and it increased up to  $300^\circ\text{C}$  (hold for 2 min) with a heating rate of  $5^\circ\text{C}/\text{min}$ . The injector temperature was set at  $250^\circ\text{C}$ , and the injection volume was 1.0  $\mu\text{L}$ . The carrier gas was helium.

To evaluate the apparent quantum efficiency (AQE) of  $\text{CeO}_2$  QDs/ $\text{BiOX}$  ( $X = \text{Cl}, \text{Br}$ ) heterostructures, a 420 nm monochromatic LED lamp (100 W) was used. The AQE was estimated as the ratio of the rate of electron consumption from the rate of  $\text{Cr}^{6+}$  reduction to the flux of incident photons, assuming that three photons are required, according to the stoichiometry of the reaction: [25]



Therefore, the AQE of  $\text{Cr}^{6+}$  reduction was calculated based on the following equation: [26,27]

$$\text{AQY}(\%) = \frac{3n_{\text{Cr}^{3+},t}N_Ahc}{PS\lambda t} \quad (2)$$

where  $n_{\text{Cr}^{3+},t}$  (mol) indicates the number of  $\text{Cr}^{3+}$  evolved during the irradiation time,  $N_A$  is Avogadro's constant,  $h$  (J·s) is Planck's constant,  $c$

( $\text{m}\cdot\text{s}^{-1}$ ) is the speed of light,  $P$  ( $\text{W}\cdot\text{m}^{-2}$ ) is the power density of the incident monochromatic light (420 nm),  $S$  ( $\text{m}^2$ ) is the irradiation area,  $\lambda$  is the wavelength of irradiated monochromatic light (420 nm) and  $t$  (s) indicates the irradiation time.

#### 2.4. Electrochemical measurements

The photoelectrochemical measurements were collected on an electrochemical workstation (CHI760E, Shanghai) in a standard three electrode system. The as-prepared sample coated onto the FTO electrode was served as the working electrode with an active area of ca.  $1.00\text{ cm} \times 1.00\text{ cm}$ , an Ag/AgCl (saturated KCl) as the reference electrode, and a Pt foil as the counter electrode. The  $\text{Na}_2\text{SO}_4$  (0.1 M) solution and 300 W Xe lamp (with a 420 nm cut off filter) were employed as electrolyte and visible light source, respectively.

### 3. Results and discussion

#### 3.1. Structure and morphology

Typical XRD patterns of the as-prepared samples are displayed in Fig. 2. For pure  $\text{BiOCl}$ , every diffraction peaks were matched well with the typical  $\text{BiOCl}$  phase (JCPDS No. 06-0249) [28]. Meanwhile, all the peaks of pure  $\text{BiOBr}$  could be easily indexed into crystal planes of  $\text{BiOBr}$  phase (JCPDS No. 09-0393) in the XRD pattern [29]. The strong and



sharp peaks indicated the high crystallinity of the BiOX ( $X = \text{Cl}, \text{Br}$ ) samples. In the case of  $\text{CeO}_2/\text{BiOX}$  ( $X = \text{Cl}, \text{Br}$ ) heterojunctions, four strong diffraction peaks with  $2\theta$  at  $28.6^\circ$ ,  $33.1^\circ$ ,  $47.5^\circ$  and  $56.4^\circ$  could be ascribed to the cubic phase  $\text{CeO}_2$  (JCPDS No. 43-1002), corresponding to the major (111), (200), (220) and (311) planes [30]. For  $\text{CeO}_2/\text{BiOCl}$  heterojunctions, the characteristic peaks of  $\text{CeO}_2$  were not obvious owing to the relatively weak crystallization and low content of  $\text{CeO}_2$ . Meanwhile, the  $\text{CeO}_2/\text{BiOBr}$  samples showed a compound of  $\text{CeO}_2$  phase and  $\text{BiOBr}$  phase, and no other peaks from possible impurities were detected in XRD patterns, revealing that the mixtures were mainly composed of  $\text{CeO}_2$  and  $\text{BiOBr}$ . Moreover, with the increase in the content of  $\text{CeO}_2$ , the diffraction peak intensities of  $\text{CeO}_2$  continuously increased, as well as the crystallinity of  $\text{BiOBr}$  decreased, which might affect the photocatalytic activity of  $\text{CeO}_2/\text{BiOBr}$  heterojunctions. In addition, the enlarged XRD patterns in Fig. S2 illustrated the changes of (001) and (102) peaks of  $\text{CeO}_2/\text{BiOCl}$  and  $\text{CeO}_2/\text{BiOBr}$ , respectively. It was clear that the diffraction peaks gradually shifted to a larger  $2\theta$  angle with the increasing content of  $\text{CeO}_2$ . Based on the closely similar or comparable in radii and charge characteristics of  $\text{Ce}^{3+}$  ( $1.01 \text{ \AA}$ ) and  $\text{Bi}^{3+}$  ( $1.03 \text{ \AA}$ ), we assumed that a small number of  $\text{Ce}^{3+}$  ions were likely to enter into the crystal lattices of  $\text{BiOX}$  ( $X = \text{Cl}, \text{Br}$ ) crystal lattice to cause the changes of lattice parameters. On the whole, it was confirmed that the  $\text{CeO}_2/\text{BiOX}$  ( $X = \text{Cl}, \text{Br}$ ) composites could be successfully synthesized by a facile low-temperature pathway.

The morphology and structure of the as-prepared  $\text{CeO}_2$ ,  $\text{BiOX}$  and  $\text{CeO}_2/\text{BiOX}$  ( $X = \text{Cl}, \text{Br}$ ) composites with various molar ratio of  $\text{Ce}/\text{Bi}$  were examined by FE-SEM. As shown in Fig. S3, the surface morphology of synthesized  $\text{BiOCl}$  displayed uniform foursquare-like nanoplates with an average thickness of about 80 nm and the edge-length was around 0.5–1  $\mu\text{m}$ . Analogously, the pristine  $\text{BiOBr}$  also appeared the nanoplate structure with smooth surface. Compared to the bare  $\text{BiOX}$  ( $X = \text{Cl}, \text{Br}$ ), the surfaces of  $\text{CeO}_2/\text{BiOX}$  ( $X = \text{Cl}, \text{Br}$ ) became rough that some small nanoparticles were gathered on the nanoplates, which were probably  $\text{CeO}_2$  QDs (Fig. S4 and Fig. S5). Meanwhile, it could be found that the number of nanoparticles increased gradually with the increasing amount of  $\text{Ce}(\text{NO}_3)_3 \cdot 6\text{H}_2\text{O}$  in the reaction system, and the aggregation of  $\text{CeO}_2$  QDs was more serious on the nanoplates, leading to the grown size. No obvious changes in the morphology of the samples were noticed after coupling with  $\text{CeO}_2$  QDs, which was in agreement with the XRD results. It was worthy of note that the pure  $\text{CeO}_2$  presented a bulk structure with a huge size about 20  $\mu\text{m}$  (Fig. S3e). Nevertheless, the size of  $\text{CeO}_2$  was overwhelmingly decreased in the systems of  $\text{CeO}_2/\text{BiOX}$  ( $X = \text{Cl}, \text{Br}$ ) hybrids which prepared by a low-temperature method. The primary reason for this phenomenon was attributed to the fact that the nucleation rate and growth rate of  $\text{CeO}_2$  crystal were far more slowly than that of  $\text{BiOX}$  ( $X = \text{Cl}, \text{Br}$ ) in the reaction process (Fig. 1). On the other hand, the pre-adsorption of  $\text{Ce}^{3+}$  onto the  $\text{BiOX}$  ( $X = \text{Cl}, \text{Br}$ ) surface would also restrict the constant growth of  $\text{CeO}_2$ . As shown in Fig. S6, the EDS spectra of  $\text{CeO}_2/\text{BiOX}$  ( $X = \text{Cl}, \text{Br}$ ) samples appeared Ce element besides Bi, O, Cl and Br, respectively. Moreover, the mapping images revealed that these elements were homogeneous distributed in the sample (Fig. S7).

Further information regarding 0.10CBC and 0.05CBB samples could be acquired from TEM and HRTEM images. It could be seen clearly that the  $\text{CeO}_2$  QDs were intimately attached onto the surfaces of  $\text{BiOCl}$  and  $\text{BiOBr}$  nanoplates (Fig. 3). The HRTEM images of 0.10CBC and 0.05CBB all exhibited a lattice spacing of 0.312 nm, corresponding to (111) plane of  $\text{CeO}_2$  (Fig. 3c and f). Meanwhile, the other interplanar distances were calculated to be 0.275 and 0.277 nm, which could be well matched to the (110) crystal plane of the  $\text{BiOCl}$  and the (110) crystal plane of the  $\text{BiOBr}$ , respectively. The intimately contacted interface would contribute to the separation of the photogenerated charge carriers.

The XPS spectra of 0.10CBC and 0.05CBB were measured to verify the surface elemental composition and chemical states. Fig. 4a displays the wide XPS spectrum of 0.10CBC and 0.05CBB, which only consists of the elements C, Bi, O, Cl/Br and Ce. The C 1s peak is attributed to the

adventitious carbon from the XPS instrument itself. In Fig. 4b, two individual XPS signals of Bi 4f were observed at binding energies of 159.4 and 164.7 eV, which can be assigned to  $\text{Bi } 4f_{7/2}$  and  $\text{Bi } 4f_{5/2}$  for the  $\text{Bi}^{3+}$  in  $\text{BiOCl}$  [31]. Nevertheless, when the  $\text{CeO}_2$  QDs were introduced, the two peaks of  $\text{Bi}^{3+}$  shifted to 164.4 and 159.1 eV in  $\text{CeO}_2/\text{BiOX}$  ( $X = \text{Cl}, \text{Br}$ ) composites, respectively. It was reported that the bonds formed between the interfaces of two phases might help to enhance the electron concentration, and boost the electron screening effect [32]. Consequently, the shift toward lower binding energy could be assigned to the improved electron concentration caused by the formation of the  $\text{CeO}_2$  QDs/ $\text{BiOX}$  ( $X = \text{Cl}, \text{Br}$ ) heterojunctions. Moreover, the O 1s spectrum (Fig. 4c) of 0.10CBC and 0.05CBB could be deconvoluted into two peaks with binding energies of 529.9, and 532.0 eV, in which the former should be assigned to Bi-O bond of  $\text{BiOX}$  ( $X = \text{Cl}, \text{Br}$ ) while the latter should be indexed to Ce-O bond of  $\text{CeO}_2$  crystal structures, respectively. Interestingly, the Ce 3d spectrum could be fitted into eight peaks labeled as V, V', V'', V''', U, U', U'' and U''' (Fig. 4d), where V and U referred to the spin-orbit coupling  $3d_{5/2}$  and  $3d_{3/2}$ , respectively. The peaks of V, V'', V''', U, U'' and U''' were at 898.29, 884.82, 882.43, 917.08, 903.62 and 900.83 eV correspond to the characteristics of  $\text{Ce}^{4+}$ , and the other signals of V' and U' (888.88, 908.42 eV) could be assigned to  $\text{Ce}^{3+}$  [33]. Meanwhile, the high-resolution scan XPS spectrum of Ce 3d in  $\text{CeO}_2$  was examined, as shown in Fig. S9a. Obviously, the signals of V' and U' also appeared in the spectrum of  $\text{CeO}_2$ , attributing to the fact that low-temperature-processed  $\text{CeO}_2$  also contained significant amount of  $\text{Ce}^{3+}$  ions in its structure. Therefore, the relative contributions of  $\text{Ce}^{3+}$  and  $\text{Ce}^{4+}$  in  $\text{CeO}_2$ , 0.10CBC and 0.05CBB could be estimated by comparing the peak areas of  $\text{Ce}^{3+}$  and  $\text{Ce}^{4+}$  in the XPS spectra as follows: [34]

$$[\text{Ce}^{3+}] = \frac{A(\text{Ce}^{3+})}{A(\text{Ce}^{3+}) + A(\text{Ce}^{4+})} \quad (3)$$

$$[\text{Ce}^{4+}] = \frac{A(\text{Ce}^{4+})}{A(\text{Ce}^{3+}) + A(\text{Ce}^{4+})} \quad (4)$$

The integrated areas of individuals XPS peaks of the Ce3d from  $\text{CeO}_2$ , 0.10CBC and 0.05CBB are listed in Table S1, and the content ratios of  $\text{Ce}^{3+}$  and  $\text{Ce}^{4+}$  are calculated and showed in Table S2. By this way, the ratios of  $\text{Ce}^{3+}$  in  $\text{CeO}_2$ , 0.10CBC and 0.05CBB were about 14.99%, 26.30% and 23.15%, respectively. It was clear that the  $\text{Ce}^{3+}$  content in  $\text{CeO}_2$  was lower than those of 0.10CBC and 0.05CBB samples. Therefore, we speculated that 11.31% and 8.16% of  $\text{Ce}^{3+}$  might be entered into the crystal lattices of 0.10CBC and 0.05CBB, respectively. As a consequence, there would generate the in-built  $\text{Ce}^{4+}/\text{Ce}^{3+}$  pair redox centers in the junctions between the surface of  $\text{CeO}_2$  QDs and  $\text{BiOX}$  ( $X = \text{Cl}, \text{Br}$ ) nanoplates, and the presence of redox couples ( $\text{Ce}^{4+}/\text{Ce}^{3+}$ ) would be beneficial for the separation and transfer of photo-excited carriers [35,36].

A plausible schematic illustration for the construction of  $\text{CeO}_2$  QDs/ $\text{BiOX}$  ( $X = \text{Cl}, \text{Br}$ ) heterostructures with the  $\text{Ce}^{4+}/\text{Ce}^{3+}$  redox centers is illustrated in Fig. 1. Considering that the melting points of  $\text{Bi}(\text{NO}_3)_3 \cdot 5\text{H}_2\text{O}$  and  $\text{Ce}(\text{NO}_3)_3 \cdot 6\text{H}_2\text{O}$  were  $30^\circ\text{C}$  and  $90^\circ\text{C}$ , and their decomposition temperature were  $75^\circ\text{C}$  and  $200^\circ\text{C}$ , respectively. The whole system was embraced in a highly reactive circumstance at molten state with the gradually increase of temperature, and the next was the decomposition of  $\text{Bi}(\text{NO}_3)_3 \cdot 5\text{H}_2\text{O}$  and  $\text{Ce}(\text{NO}_3)_3 \cdot 6\text{H}_2\text{O}$  respectively. In other words, the reaction system only appeared a short melting state during the heating process to ensure the fast diffusion of ions, and more time at  $300^\circ\text{C}$  was needed for the better growth and crystallization of  $\text{CeO}_2$  and  $\text{BiOX}$  ( $X = \text{Cl}, \text{Br}$ ). Meanwhile, some reactant gas ( $\text{NO}_x$ ) and water could be evaporated during the process, but most of the gas and steam were spilled over because of the semi-enclosed space of reaction device. Moreover, there were no obvious signals of N-related species appeared in the XPS spectra and EDS spectra of the as-prepared samples, hinting that the produced gas would not affect the fabrication of  $\text{CeO}_2/\text{BiOX}$  ( $X = \text{Cl}, \text{Br}$ ) heterostructures. Compared with the

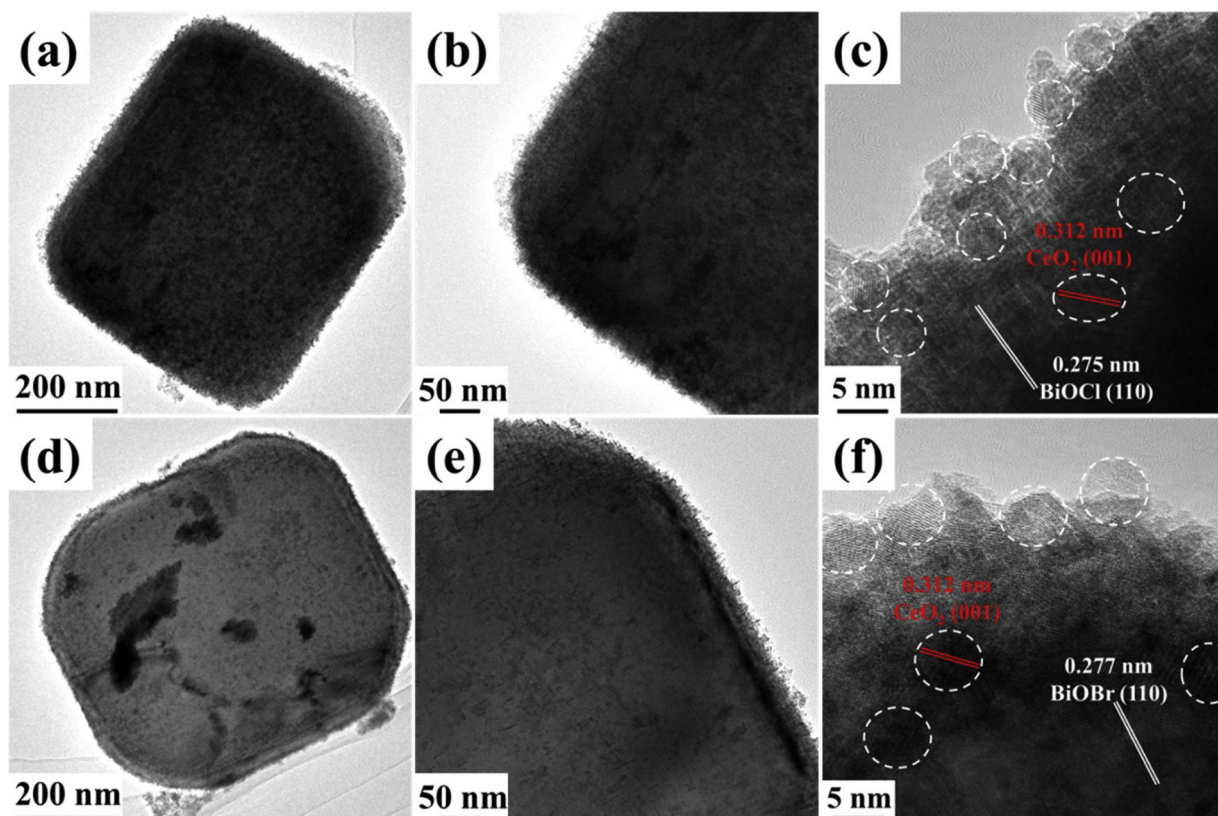


Fig. 3. TEM and HRTEM images of (a, b, c) 0.01CBC and (d, e, f) 0.05CBB.

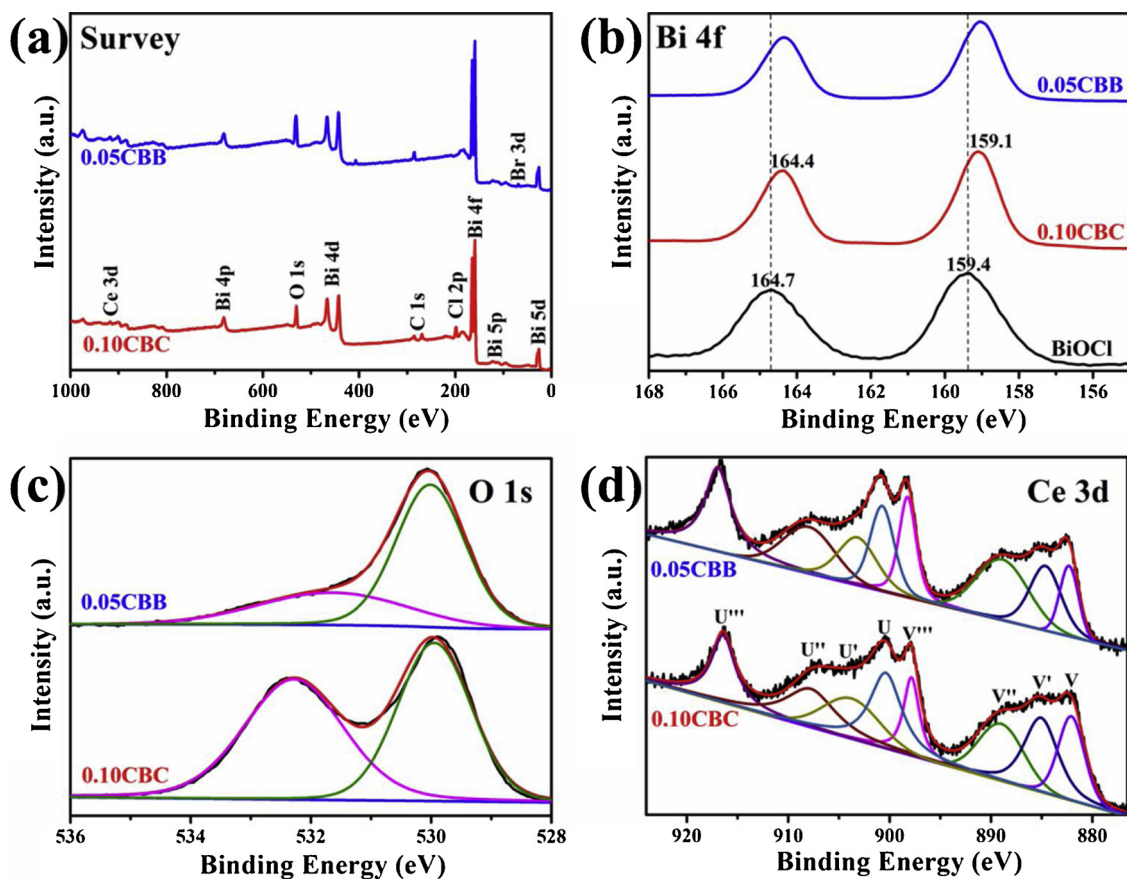


Fig. 4. XPS spectra of 0.10CBC, 0.05CBB and BiOCl. (a) the survey scan, (b) Bi 4f, (c) O 1s, and (d) Ce 3d.

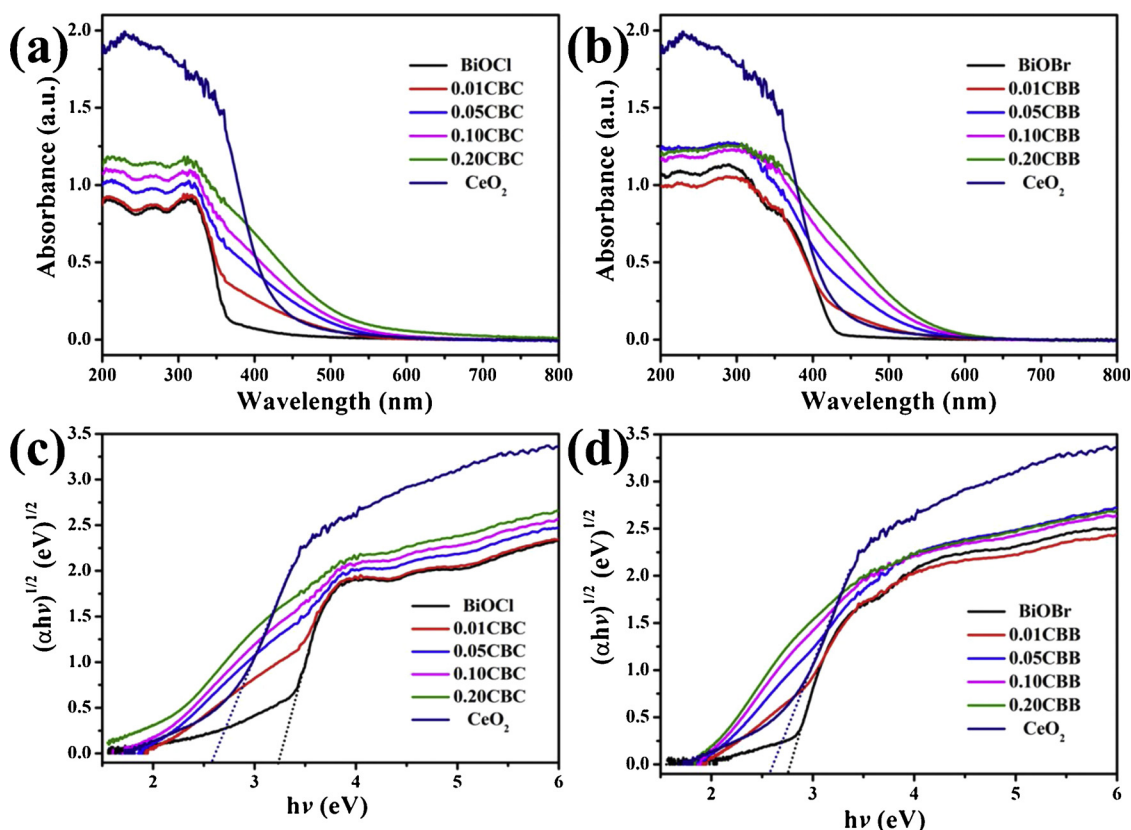


Fig. 5. (a, b) UV-vis diffuse reflectance spectra and (c, d)  $(\alpha h\nu)^{1/2}$  versus  $h\nu$  plots of pure  $\text{CeO}_2$ ,  $\text{BiOX}$  and  $\text{CeO}_2$  QDs/ $\text{BiOX}$  ( $X = \text{Cl}, \text{Br}$ ) heterostructures.

traditional high temperature solid state method or the complicated manipulation, the  $\text{CeO}_2$  QDs/ $\text{BiOX}$  ( $X = \text{Cl}, \text{Br}$ ) heterojunctions with the self-created in-built  $\text{Ce}^{4+}/\text{Ce}^{3+}$  redox centers could be synthesized successfully via a green low-temperature procedure, which benefited from the virtue of the characteristics of molten salts.

### 3.2. Optical properties

To assess the visible light absorption abilities and bandgaps of as-prepared  $\text{CeO}_2$ ,  $\text{BiOX}$ , and  $\text{CeO}_2$  QDs/ $\text{BiOX}$  ( $X = \text{Cl}, \text{Br}$ ) heterojunctions samples, the UV-vis diffuse reflectance spectra (DRS) were investigated, as shown in Fig. 5a and b. Obviously, the pristine  $\text{BiOCl}$  nanoplates only undergo photoabsorption in the UV light region, as well as the absorbance in the visible region was negligible, while the  $\text{CeO}_2$  and  $\text{BiOBr}$  samples displayed little visible-light-response ability. The limited absorption of visible light could severely restrict their photocatalytic performance. As for the  $\text{CeO}_2$ / $\text{BiOX}$  ( $X = \text{Cl}, \text{Br}$ ) samples, they all exhibited a wide photoabsorption from UV to visible light, and the absorption edge was gradually extended with the increasing of  $\text{CeO}_2$  amount, indicating decreased band-gap energies. Interestingly, compared with  $\text{CeO}_2$ , the CBC and CBB samples displayed a further enhancement for the optical absorption in the visible regions, which could be attributed to the interactions between the tightly-coupled surface of  $\text{CeO}_2$  QDs and  $\text{BiOX}$  ( $X = \text{Cl}, \text{Br}$ ) nanoplates (via the formed heterojunctions). The enhanced harvest in visible light region might contribute to more photogenerated electrons and holes and then result in the favorably improved photocatalytic activity. Furthermore, the optical images of as-prepared samples are exhibited in Fig. S10. Obviously, the color of  $\text{BiOCl}$  and  $\text{BiOBr}$  were white and faint yellow respectively, and the color of  $\text{CeO}_2$  QDs/ $\text{BiOX}$  ( $X = \text{Cl}, \text{Br}$ ) samples changed from faint yellow to deep yellow with the increase in content of  $\text{CeO}_2$ . It was worth noting that the alteration of light absorption was in keeping with the color diversification of the photocatalysts.

Considering that both of  $\text{BiOCl}$  [37],  $\text{BiOBr}$  [38] and  $\text{CeO}_2$  [39] are indirect band gap semiconductors, the derived band gaps of as-synthesized samples could be obtained from the intercept of the tangents to the plots of  $(\alpha h\nu)^{1/2}$  vs. photon energy ( $h\nu$ ) [40]. As displayed in Fig. 5c and d, the calculated band gaps of  $\text{BiOCl}$ ,  $\text{BiOBr}$  and  $\text{CeO}_2$  were 3.24 eV, 2.74 eV and 2.57 eV, respectively.

To further make a thorough inquiry for the energy band structures of as-prepared samples, the Mott-Schottky curve was carried out where it could be used to conclude the flat band potential and donor density of semiconductor, as shown in Fig. 6. The positive slopes indicated that  $\text{BiOCl}$ ,  $\text{BiOBr}$  and  $\text{CeO}_2$  were all n-type semiconductors [41], so the formed  $\text{CeO}_2$ / $\text{BiOX}$  composites belong to the p-p type heterojunctions. Moreover, the values of the flat band potential were obtained from the Mott-Schottky equation [42]:

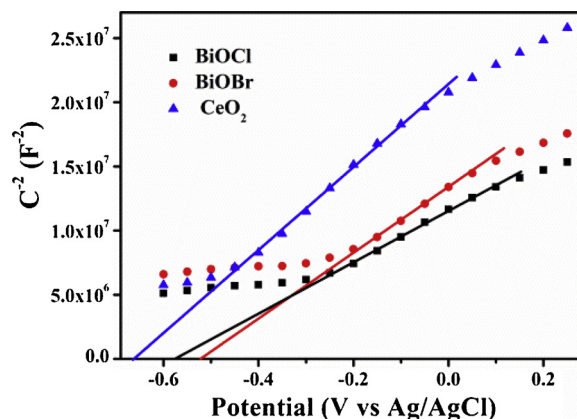


Fig. 6. Mott-Schottky plots of  $\text{BiOCl}$ ,  $\text{BiOBr}$  and  $\text{CeO}_2$ .



$$\frac{1}{C^2} = \frac{2}{e\epsilon\epsilon_0 N_D} (E - E_{fb} - \frac{KT}{e}) \quad (5)$$

where  $C$  is the capacitance of the space charge layer,  $e$  is the electronic charge,  $\epsilon$  and  $\epsilon_0$  are the dielectric constants of free space and the semiconductor, respectively.  $N_D$  is the donor density,  $K$  is Boltzmann's constant,  $T$  is the temperature,  $E$  is the applied potential,  $E_{fb}$  is the flat-band potential [43]. From Fig. 6,  $E$  values (linear intersection) were estimated to be -0.58, -0.52, and -0.66 V (vs Ag/AgCl) for BiOCl, BiOBr and CeO<sub>2</sub>. As the value of  $KT/e = 0.0257$ ,  $E$  (NHE) =  $E$  (Ag/AgCl) + 0.197 eV, so the corresponding flat band potentials ( $E_{fb}$ ) of BiOCl, BiOBr and CeO<sub>2</sub> were estimated to be -0.41, -0.35, and -0.49 V (vs NHE). There is widely accepted that the conduction band potentials ( $E_{CB}$ ) of n-type semiconductors are approximately 0–0.2 eV higher than that of the  $E_{fb}$  [43]. In this case, the difference was set to be 0.1 eV, so the  $E_{CB}$  values were -0.51, -0.45 and -0.59 eV for BiOCl, BiOBr and CeO<sub>2</sub>, respectively. Based on the formula  $E_{CB} = E_{VB} - E_g$  [44], the  $E_{VB}$  values of BiOCl, BiOBr and CeO<sub>2</sub> were estimated to be 2.72, 2.29 and 1.98 eV.

### 3.3. Photocatalytic activity evaluation

The photocatalytic performances based on two series of CeO<sub>2</sub> QDs/BiOX ( $X = \text{Cl, Br}$ ) samples were systematically investigated for the photocatalytic degradation of TC under 5 W white LED light irradiation, and the results were collected when the adsorption equilibrium of the contaminants on the photocatalysts powders. As shown in Fig. 7, the blank experiments without the catalysts suggested that the self-degradation TC was very limited and negligible under the visible light irradiation. Fig. 7a depicts the photodegradation of TC with BiOX ( $X = \text{Cl, Br}$ ), 0.10CBC, 0.05CBB and CeO<sub>2</sub>. It was vividly shown that the individual BiOCl possessed a poor visible light photocatalytic

performance because of the weak visible light absorption, originating from the wide band gap (3.23 eV). Meanwhile, the pure BiOBr and CeO<sub>2</sub> also exhibited relatively low photocatalytic performance for TC degradation and only 62% and 46% of TC could be removed, while the TC removal efficiency of 0.05CBB could reach 97% after 2 h under visible light irradiation. On the other hand, the photocatalytic performances of CeO<sub>2</sub> QDs/BiOX ( $X = \text{Cl, Br}$ ) heterojunctions for the degradation of TC with different mole ratios of Ce/Bi are displayed in Fig. S11, it was worth noting that 0.10CBC and 0.05CBB samples revealed the highest photocatalytic activity for the degradation of TC among the CeO<sub>2</sub>/BiOCl and CeO<sub>2</sub>/BiOBr systems, respectively. In addition, the photocatalytic action spectra of 0.05CBB were recorded under the 100 W LED monochromatic light (365 nm, 420 nm and 495 nm) irradiated for 15 min (Fig. 8a). Obviously, the monochromatic photocatalysis action spectra of 0.05CBB were concordant with its UV-Vis absorption spectrum, and the 0.05CBB exhibited efficient photocatalytic performance when the incident photon energy was larger than its bandgap. With the decrease of photon energy, the catalytic rate was significantly reduced owing to the insufficient excitation. Moreover, the photocatalytic performances for the RhB degradation of as-prepared photocatalysts were also explored to investigate the organic dye degradation, as shown in Fig. S12. Obviously, the CeO<sub>2</sub> QDs/BiOX ( $X = \text{Cl, Br}$ ) composites also exhibited the superior removal efficiency of RhB to that of solitary CeO<sub>2</sub>, BiOCl and BiOBr. As expected, the efficient photocatalytic activity of CeO<sub>2</sub> QDs/BiOX ( $X = \text{Cl, Br}$ ) heterojunctions illustrated the effectiveness and feasibility of the proposed procedure.

The identification of active species is particularly important for the photocatalytic mechanism, and the trapping experiment was used to ascertain the reactive species produced during the TC degradation process. Herein, the ammonium oxalate (AO), isopropanol (IPA) and benzoquinone (BQ) were used as the scavengers for  $h^+$ ,  $\cdot\text{OH}$  and  $\cdot\text{O}_2^-$ , respectively [45,46]. Fig. 7d shows the photocatalytic degradation of

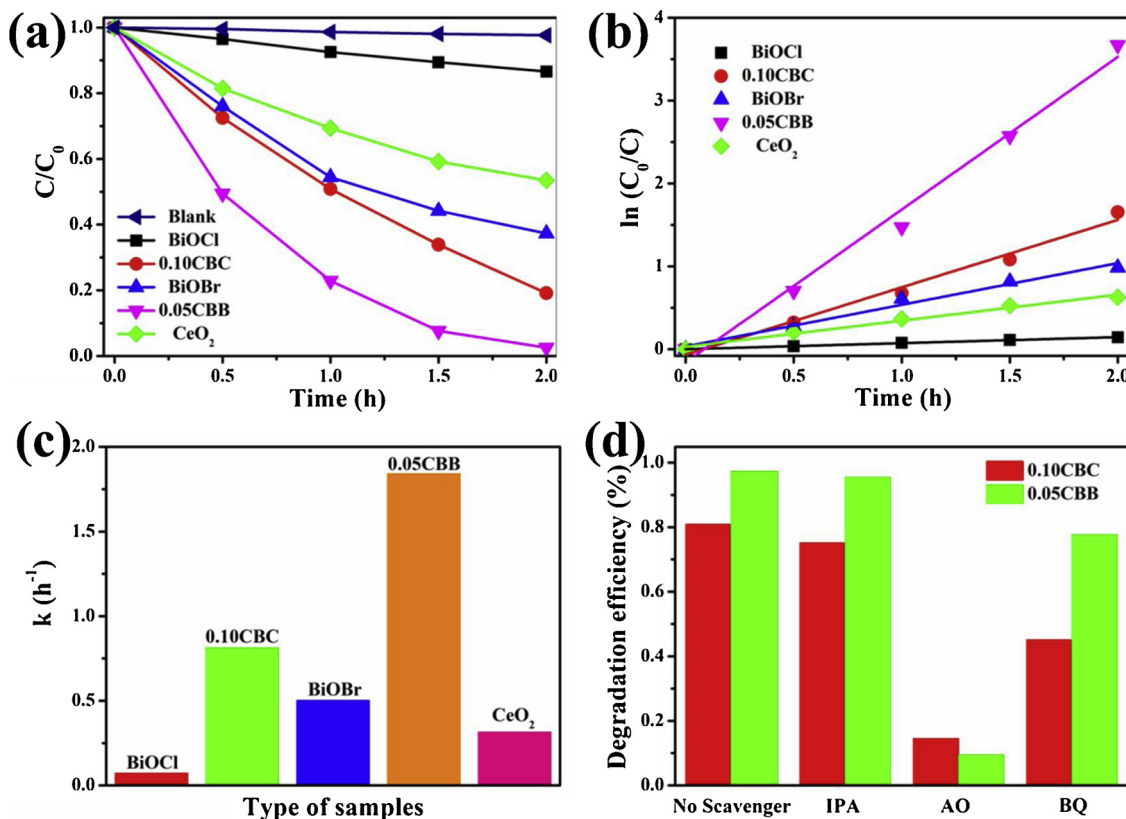


Fig. 7. (a) The photocatalytic degradation curves, (b) the pseudo-first-order kinetics curves and (c) comparison of the corresponding  $k$  values for degradation of TC over the as-prepared samples under 5 W white LED light irradiation, (d) The effects of different scavengers on the TC degradation process over 0.10CBC and 0.05CBB samples.

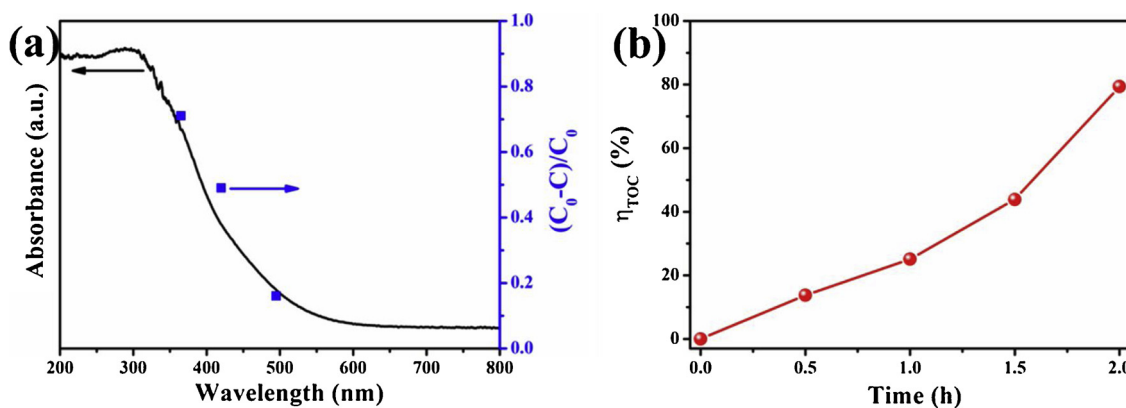


Fig. 8. (a) The UV-vis absorption spectrum and photocatalytic action spectra of 0.05CBB, (b) TOC removal curve of the 0.05CBB under 5 W white LED light irradiation.

TC over 0.10CBC and 0.05CBB with different quenchers. Obviously, the introduction of IPA had slightly affected the photodegradation of TC, indicating that  $\cdot\text{OH}$  was hardly able to generate and it was not an important contributor in the degradation process. Whereas, it was worth noting that there was a partial decrease of degradation rate with the addition of BQ. Meanwhile, the degradation of TC was greatly inhibited in the presence of AO. Consequently, the  $\text{h}^+$  was the dominating active species while the  $\text{O}_2^{\cdot-}$  served as a secondary factor in decomposition process of TC. In other words, TC was mainly degraded by the photocatalytic oxidation capacity of  $\text{CeO}_2$  QDs/BiOX ( $\text{X} = \text{Cl}, \text{Br}$ ) heterojunctions under the visible light irradiation.

To explore the mineralization of TC, the TOC analyses of 0.05CBB were conducted in Fig. 8b. Obviously, the TC was gradually mineralized into  $\text{CO}_2$  and  $\text{H}_2\text{O}$  with the extension of illumination time, indicated that the as-prepared  $\text{CeO}_2$  QDs/BiOX ( $\text{X} = \text{Cl}, \text{Br}$ ) heterojunctions displayed great potential for environmental applications. Moreover, it was worthy of note that the removal rate of TOC (79.36%) was significantly lower than the degradation rate (97.46%) toward TC degradation within 2 h, which suggested that it was easier to destroy the organic group of TC rather than to mineralize it into  $\text{CO}_2$  and  $\text{H}_2\text{O}$ . As expected from the complexity of TC molecular structure, there would be numerous intermediates formed and then destroyed in the photocatalytic oxidation process of  $\text{CeO}_2$  QDs/BiOX ( $\text{X} = \text{Cl}, \text{Br}$ ) heterojunctions. In order to gain much insight into the degradation pathway and mechanism, the possible oxidation byproducts were identified by GC-MS. Fig. S13 presents the total ion chromatograms (TIC) of GC-MS of TC solution after the photocatalytic experiment, and the retention time and possible molecular structures of main intermediates are also summarized in Table 1. Since the electron density of double bond at C11a-C12 position was higher than that of benzene ring and might be preferentially attacked by active species, the TC could be transformed into the intermediate with  $m/z = 461$  at the C11a-C12 position [47]. Meanwhile, the formation of a compound with  $m/z = 416$  could be formed due to lose two methyl groups of TC, and the generation of intermediate with  $m/z = 400$  was proposed to occur via losing hydroxyl group in C3 [48]. Moreover, other intermediates of lower molecular weight were mainly derived through the ring-opening reactions, and following by the cleavage of the central carbon [49]. With the further oxidation of  $\text{h}^+$ , those intermediates were degraded and finally evolved to  $\text{CO}_2$ ,  $\text{H}_2\text{O}$  and  $\text{NH}_3$ . Summarizing the above mentioned results, the proposed photocatalytic oxidation pathways of TC were speculated in Fig. 9.

In order to further reconnoiter the photocatalytic reduction performance of as-prepared samples,  $\text{Cr}^{6+}$  was chosen to act as a probe pollutant. Fig. 10a presents the variation of  $\text{Cr}^{6+}$  concentration ( $\text{C}/\text{C}_0$ ) over prepared samples as the function of reaction time. After 1 h irradiation, the photoreduction rates of  $\text{Cr}^{6+}$  over  $\text{CeO}_2$ , BiOCl, 0.10CBC, BiOBr and 0.05CBB photocatalysts were 49%, 7%, 57%, 40% and 97%,

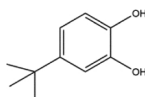
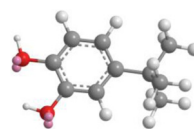
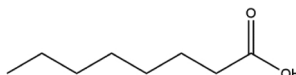
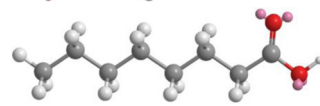
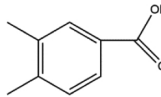
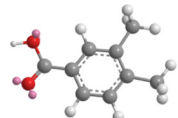
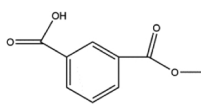
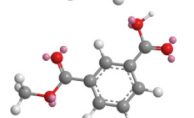
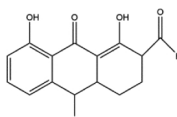
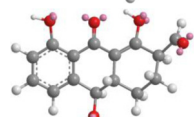
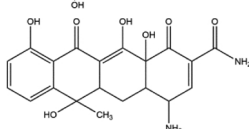
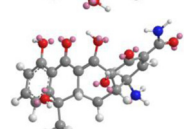
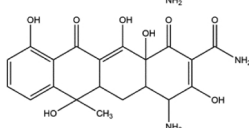
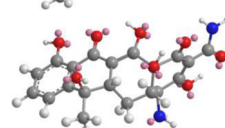
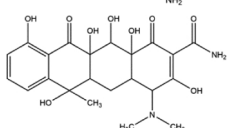
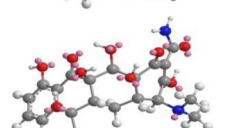
respectively. It was clear that the 0.05CBB sample possessed the inconceivable photocatalytic reduction activity among these samples, and the formation of  $\text{CeO}_2$  QDs/BiOX ( $\text{X} = \text{Cl}, \text{Br}$ ) heterojunctions could significantly speed up the process of photocatalytic reduction of  $\text{Cr}^{6+}$ . The results were similar to the photocatalytic degradation of TC and RhB, 0.10CBC and 0.05CBB samples also revealed the optimum photocatalytic reduction activity in the series of  $\text{CeO}_2$ /BiOCl and  $\text{CeO}_2$ /BiOBr samples, respectively (Fig. S14). Moreover, the calculated AQY for  $\text{Cr}^{6+}$  reduction by 0.05CBB was about ca. 3.07% during 15 min 420 nm monochromatic LED (100 W) light irradiation. Apparently, the prepared heterojunctions still owned the excellent visible-light-driven photocatalytic reduction and oxidation activities even under the light irradiation of a low power lamp, which was meaningful for the practical application of photocatalysts under solar light.

As shown in Figs. 7b and 10b, the photocatalytic reaction processes of TC degradation and  $\text{Cr}^{6+}$  reduction over as-prepared samples followed pseudo-first-order kinetics owing to good linearity of the corresponding  $\ln(\text{C}_0/\text{C})$  plots, and the slope of the fitting line was consistent with the value of rate constant ( $k$ ). Fig. 7c described that the 0.05CBB exhibited the inapproachable photocatalytic ability toward TC degradation with a  $k$  value of  $1.8421 \text{ h}^{-1}$ , which were 5.86 and 3.66 times than that of pure  $\text{CeO}_2$  ( $0.3144 \text{ h}^{-1}$ ) and BiOBr ( $0.5027 \text{ h}^{-1}$ ), respectively. Afterward, the  $k$  value of 0.05CBB for the photocatalytic reduction was almost 4.46 and 5.85 times larger than that of untreated  $\text{CeO}_2$  and BiOBr samples, respectively (Fig. 10c). Furthermore, the details of rate constants  $k$  and correlation coefficients  $R^2$  for photodegradation and reduction over the  $\text{CeO}_2$ /BiOCl and  $\text{CeO}_2$ /BiOBr are summarized in Table S3 and Table S4. Particularly, it should be noted that the photocatalytic activity of the  $\text{CeO}_2$  QDs/BiOX ( $\text{X} = \text{Cl}, \text{Br}$ ) composites was inhibited to a certain extent with the increase of  $\text{CeO}_2$  loading. This was probably owing to the excess of  $\text{CeO}_2$  QDs covering upon the surface of BiOX ( $\text{X} = \text{Cl}, \text{Br}$ ) nanoplates, which blocked the irradiation reach the surface of BiOX ( $\text{X} = \text{Cl}, \text{Br}$ ) so as to decrease the production of photogenerated carriers. In addition, the excessive  $\text{CeO}_2$  also acted as the recombination center, which accelerated the recombination of the photoinduced electron-hole pairs, as well as weaken the interfacial effect. Consequently, it could be deduced from the above results that the  $\text{CeO}_2$  QDs/BiOX ( $\text{X} = \text{Cl}, \text{Br}$ ) heterojunctions exhibited superior photocatalytic oxidation and reduction activities to that of  $\text{CeO}_2$ , BiOCl and BiOBr, attributing to the existing of  $\text{Ce}^{4+}/\text{Ce}^{3+}$  redox centers, as well as the formation of strong interfacial interaction via heterojunction among different components, which could efficiently accelerate the separation and transfer of photogenerated  $\text{h}^+$  and  $\text{e}^-$ .

For comparison, the photocatalytic oxidation and reduction abilities of P25 and N-doped P25 (N-P25) were also tested under the same conditions. As shown in Fig. S16, it was seen that the photocatalytic performances of 0.10CBC and 0.05CBB were considerably higher than that of the commercial P25 and N-P25. In addition, to check the effect



**Table 1**  
Possible degradation intermediates identified by GC–MS.

Retention time (min)	m/z	Possible structure	
8.26	166		
17.23	144		
23.63	150		
27.36	180		
35.00	274		
37.19	400		
41.28	416		
46.74	461		

of heterojunctions between  $\text{CeO}_2$  and  $\text{BiOX}$  ( $X = \text{Cl}, \text{Br}$ ) phases on photocatalytic activity, we prepared the  $\text{CeO}_2$  nanoparticles and  $\text{BiOX}$  ( $X = \text{Cl}, \text{Br}$ ) nanoplates separately (Fig. S17), then combined them to form heterojunction structures by physically mixing the  $\text{CeO}_2$  nanoparticles and  $\text{BiOCl}$  nanoplates (0.10:1 in mole ratio), as well as mixing the  $\text{CeO}_2$  nanoparticles and  $\text{BiOBr}$  nanoplates (0.05:1 in mole ratio). The XRD patterns of the mixtures were similar to those of the 0.10CBC and 0.05CBB samples (Fig. S18). However, the photocatalytic activities of the mixtures were much lower than those of the 0.10CBC and 0.05CBB heterostructures (Fig. S19), suggesting that the heterojunctions and the in-built  $\text{Ce}^{4+}/\text{Ce}^{3+}$  redox centers between the  $\text{CeO}_2$  QDs and  $\text{BiOX}$  ( $X = \text{Cl}, \text{Br}$ ) nanoplates were essentially significant in improving the photo-oxidation and reduction performance. Comparing with the above mixture heterojunctions, this green and low-temperature method could prepare the  $\text{CeO}_2$  with smaller size and better dispersibility in  $\text{CeO}_2$  QDs/ $\text{BiOX}$  ( $X = \text{Cl}, \text{Br}$ ) systems, which could afford more opportunity to connect with  $\text{BiOX}$  ( $X = \text{Cl}, \text{Br}$ ) nanoplates. Moreover, the more closely contacted interface between two components would lead to a great deal of enhancement for the separation and transfer of photoexcited charges.

Generally, the stability of photocatalyst plays a vital role in its application for practical application. 0.10CBC and 0.05CBB were employed as representative samples to investigate the stability and reusability for the degradation of TC. As shown in Fig. 11, the

photocatalytic efficiencies were slightly reduced after undergoing six repeated runs, attributing to the loss of samples during each collection and rinsing process. In addition, the crystalline structures of 0.10CBC and 0.05CBB samples after six cycles were also studied, and the results are displayed in Fig. 11b. It was clearly revealed that no significant changes happened for the position and the ratio of diffraction peaks in the corresponding XRD patterns, indicating that the  $\text{CeO}_2$  QDs/ $\text{BiOX}$  ( $X = \text{Cl}, \text{Br}$ ) heterojunctions had good reusability and structural stability for wastewater treatment under visible light irradiation.

#### 3.4. The underlying photocatalytic mechanism

It is well known that the charge dynamics property plays a pivotal role in determining the ultimate photoreactivity. PL spectra could provide significant information on the transfer and separation efficiency of photogenerated charge carriers on the surface of semiconductors because the recombination of carriers would give rise to the PL signal, indicative of the photocatalytic capability of a photocatalyst [50]. Fig. 12a presents the PL spectra of pure  $\text{BiOX}$  and  $\text{CeO}_2$  QDs/ $\text{BiOX}$  ( $X = \text{Cl}, \text{Br}$ ) heterojunctions excited at 320 nm. Apparently,  $\text{BiOCl}$  and  $\text{BiOBr}$  showed the highest intensity of emission peaks, indicating the fastest recombination rate of photogenerated electron-hole pairs. Although the main emission peaks positions of  $\text{CeO}_2$  QDs/ $\text{BiOX}$  ( $X = \text{Cl}, \text{Br}$ ) heterojunctions were similar to that of pure  $\text{BiOX}$  ( $X = \text{Cl}, \text{Br}$ ), the

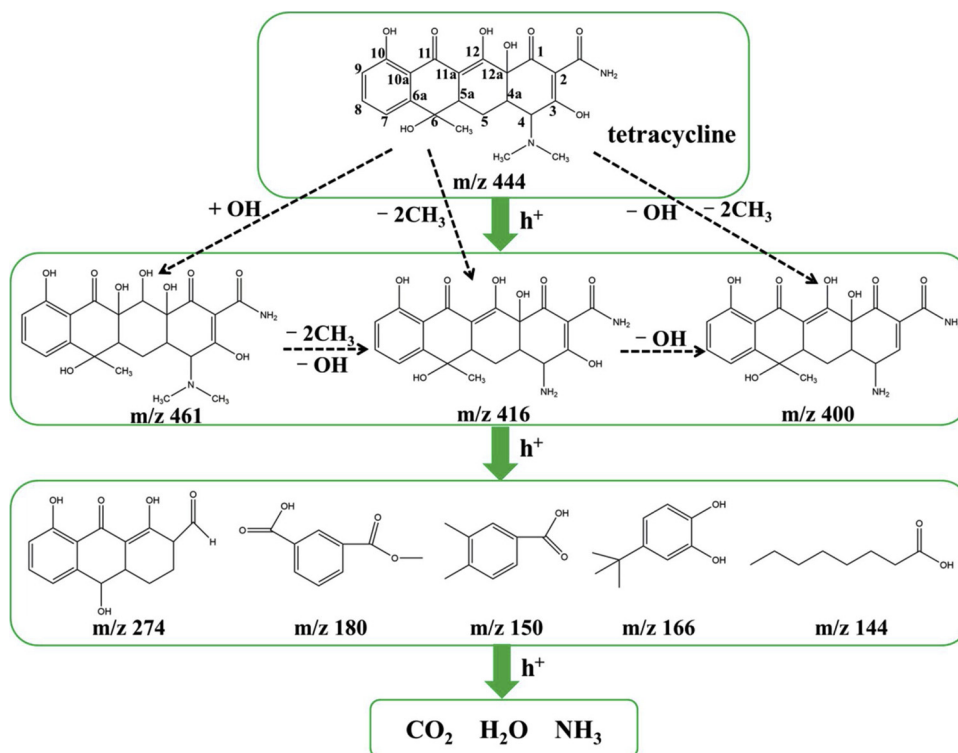


Fig. 9. The proposed photocatalytic oxidation pathways of TC.

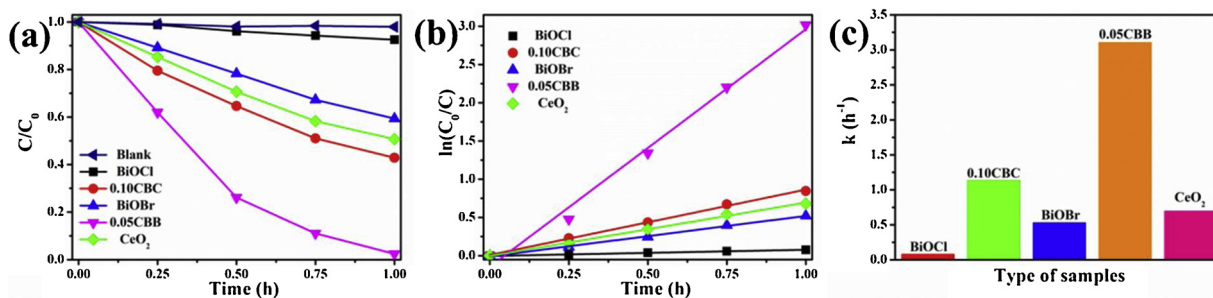
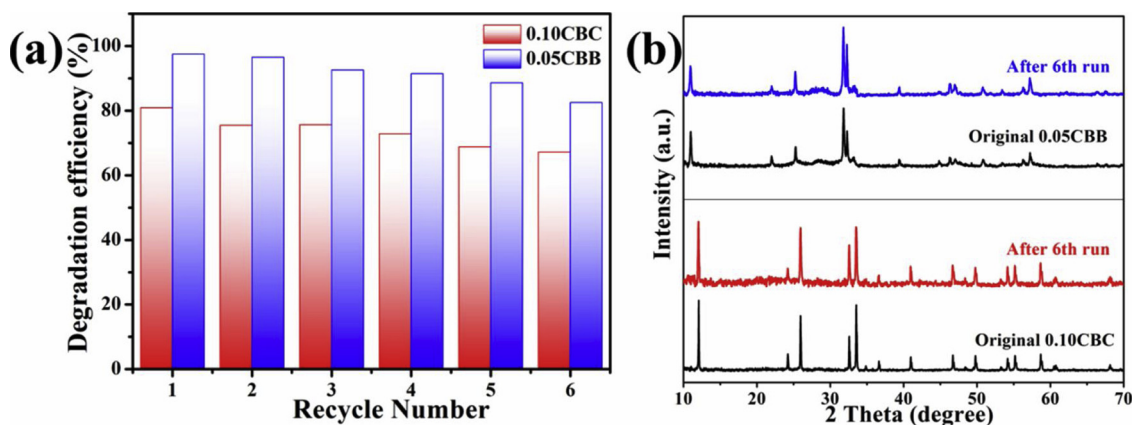
Fig. 10. (a) The photocatalytic reduction curves, (b) the pseudo-first-order kinetics curves and (c) comparison of the corresponding  $k$  values for reduction of Cr<sup>6+</sup> over the as-prepared samples under 5 W white LED light irradiation.

Fig. 11. (a) Recycling experiments and (b) XRD patterns before and after six cycles of 0.10CBC and 0.05CBB for the photocatalytic degradation of TC.

obviously decreased PL intensity of 0.10CBC and 0.05CBB could be observed, which suggested that the remarkable enhancement appeared in the separation of the photoexcited carriers with the introduction of CeO<sub>2</sub> QDs (Fig. S20).

In order to gain a deeper insight into the photo-physical characteristics of photo-induced charge carriers, the ns-level time-resolved fluorescence decay spectra of pure BiOX and CeO<sub>2</sub> QDs/BiOX (X = Cl, Br) composites are displayed in Fig. 12b and c. The decay spectra

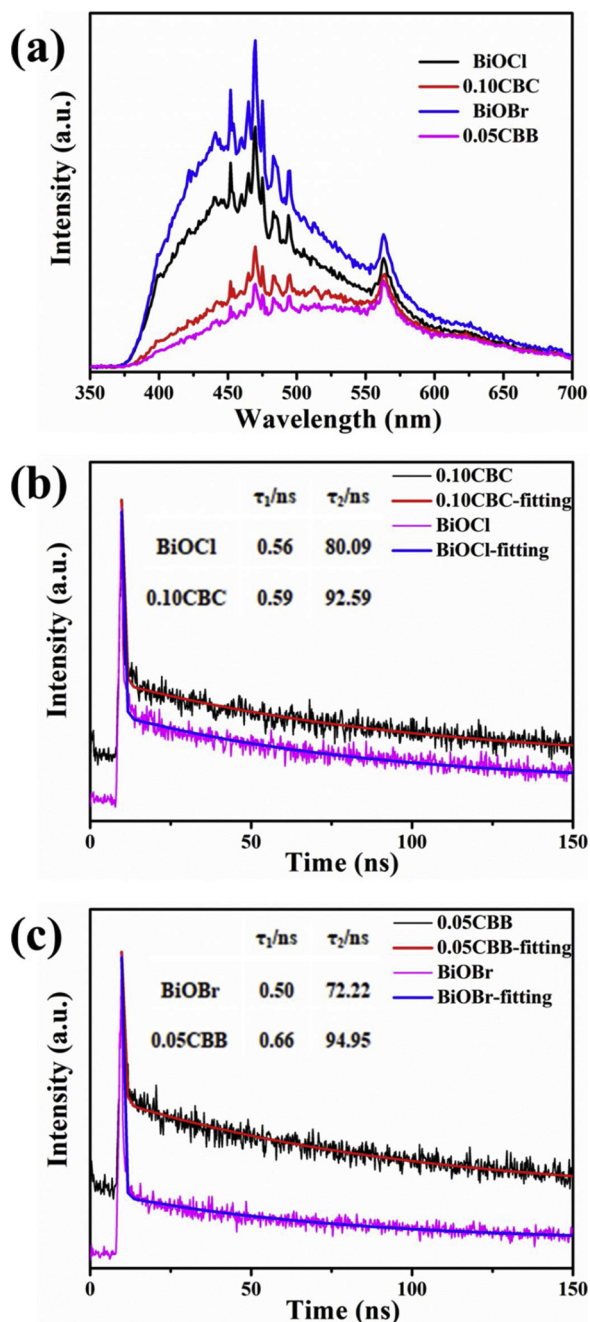


Fig. 12. (a) PL spectra, (b, c) Time-resolved fluorescence decay spectra of BiOCl, BiOBr, 0.10CBC and 0.05CBB.

indicated that the fluorescent intensities of all the samples decay exponentially, and these spectra were all well with the following biexponential function fitting equation [51]:

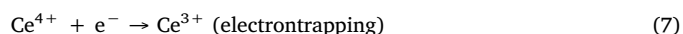
$$n(t) = A + A_1 e^{-\frac{t}{\tau_1}} + A_2 e^{-\frac{t}{\tau_2}} \quad (6)$$

where  $n(t)$  is the concentration of charge carrier,  $A$ ,  $A_1$ ,  $A_2$  are constants which obtained after fitting every decay curve,  $\tau_1$  and  $\tau_2$  are the short and long lifetime of charge carrier, respectively. The two radiative lifetime components are also listed in the inset of Fig. 12b and c. In detail, after coupling with  $\text{CeO}_2$  QDs, the short lifetime ( $\tau_1$ ) of BiOCl increased from 0.56 ns to 0.59 ns. Meanwhile, the  $\tau_2$  lifetime component of 0.10CBC was 92.59 ns, which was 12.50 ns longer than that of BiOCl. Besides, BiOBr hold lifetimes of 0.50 and 72.22 ns for the fast ( $\tau_1$ ) and slow ( $\tau_2$ ) components, respectively. Note that 0.05CBB had longer lifetimes for both components, with 0.66 ns fitted for  $\tau_1$  and

94.95 ns for  $\tau_2$ . Clearly, in contrast to the pure BiOCl and BiOBr, the  $\text{CeO}_2$  QDs/BiOX ( $X = \text{Cl, Br}$ ) heterojunctions disclosed slower decay kinetics. In other word, the life times of the charge carriers over  $\text{CeO}_2$  QDs/BiOX ( $X = \text{Cl, Br}$ ) nanoplates were longer than that of the untreated BiOX ( $X = \text{Cl, Br}$ ) [52]. The prolonged lifetime of  $\tau_1$  and  $\tau_2$  was related to the enhanced electron trapping and electron-hole recombination induced by the close contact heterojunctions effect and the  $\text{Ce}^{4+}/\text{Ce}^{3+}$  redox centers [53]. As expected, the greatly enhancement of efficient charge separation achieved in the  $\text{CeO}_2$  QDs/BiOX ( $X = \text{Cl, Br}$ ) heterojunctions.

The transient photocurrent responses for BiOX and  $\text{CeO}_2$  QDs/BiOX ( $X = \text{Cl, Br}$ ) nanoplates were also carried out under visible irradiation through light-on and light-off cycles for further proving PL conclusion. As shown in Fig. 13a, it was clear that the photocurrent responses of pure BiOCl and BiOBr were quite low, which might come from the fast recombination of electron-hole pairs. Compared with pure BiOX ( $X = \text{Cl, Br}$ ), 0.10CBC and 0.05CBB composites could generate considerably enhanced photocurrent density, in which the higher photocurrent represents a longer life of photogenerated carriers and better separation efficiency of electron-hole pairs. This designated  $\text{CeO}_2$ -loading accelerated the transfer of the photo-generated carriers at the interface between  $\text{CeO}_2$  QDs and BiOX ( $X = \text{Cl, Br}$ ) nanoplates. Meanwhile, for the purpose of further exploration about the electron transfer process, the electrochemical impedance spectroscopy (EIS) was conducted (Fig. 13b). The EIS of the 0.10CBC and 0.05CBB showed smaller semicircle radius than that of others, indicating that  $\text{CeO}_2$  QDs/BiOX ( $X = \text{Cl, Br}$ ) heterojunctions owned a more efficient and faster charge separation. Profit from the existing of  $\text{Ce}^{4+}/\text{Ce}^{3+}$  redox centers and the close contact junctions,  $\text{CeO}_2$  QDs/BiOX ( $X = \text{Cl, Br}$ ) hybrids were more capable of producing charge carriers, harvesting light and separating electron-hole pairs, thereby improving the visible light photocatalytic activity.

According to the above investigations and band structures of BiOCl, BiOBr and  $\text{CeO}_2$ , the tentative mechanisms for charge separation process of the  $\text{CeO}_2$ /BiOCl and  $\text{CeO}_2$ /BiOBr heterostructures are proposed in Fig. 14. It is acknowledged that the formation of heterojunction would as an essential bridge for the separation and transfer of photo-generated carriers. For the  $\text{CeO}_2$ /BiOCl heterojunction photocatalysts, under visible light irradiation, the  $e^-$  at the valence band (VB) of BiOCl could not be excited to the conduction band (CB) owing to the wide band gap energy. Meanwhile, the photoexcited  $e^-$  produced on the VB of  $\text{CeO}_2$  could be immediately excited to the CB of  $\text{CeO}_2$ , and eventually injected to the CB of BiOCl, leaving behind the  $h^+$  in the VB of  $\text{CeO}_2$  according to the principle of charge conservation. When  $\text{CeO}_2$ /BiOBr hybrids were subjected to visible light irradiation, both of  $\text{CeO}_2$  and BiOBr could easily be excited, generating the  $e^-$  and  $h^+$  pairs. Since the CB and VB of BiOBr were lower than that of  $\text{CeO}_2$ , the photogenerated  $e^-$  on the CB of  $\text{CeO}_2$  would be transferred easily into the CB of BiOBr. Simultaneously, the photoexcited  $h^+$  from BiOBr would migrate to the VB of  $\text{CeO}_2$ . Most importantly, the in-built  $\text{Ce}^{4+}/\text{Ce}^{3+}$  redox centers formed in the  $\text{CeO}_2$  QDs/BiOX ( $X = \text{Cl, Br}$ ) composites might act as efficient scavengers to trap the transfer  $e^-$ , boosting photogenerated charge separation and suppress recombination. In detail, most part of photoinduced  $e^-$  on the CB of  $\text{CeO}_2$  would move into the CB of BiOX ( $X = \text{Cl, Br}$ ), and the others were trapped by  $\text{Ce}^{4+}$  ions, which  $\text{Ce}^{4+}$  ions could be reduced to  $\text{Ce}^{3+}$  ions [54]. Nevertheless, the  $\text{Ce}^{3+}$  ions have the unfilled  $4f^1$  orbital and become relatively unstable than the  $\text{Ce}^{4+}$  ions. Hence, the  $\text{Ce}^{3+}$  ions could easily returned to the original stable state ( $\text{Ce}^{4+}$ ) by transferring  $e^-$  to absorbed  $\text{O}_2$  on the surface of  $\text{CeO}_2$  QDs/BiOX ( $X = \text{Cl, Br}$ ) nanoplates [35,36]. Meanwhile, the adsorbed  $\text{O}_2$  was reduced to  $\cdot\text{O}_2^-$  radical, which could further degrade TC and RhB. In other words, the presence of in-built  $\text{Ce}^{4+}/\text{Ce}^{3+}$  redox centers might expedite the following reaction process:





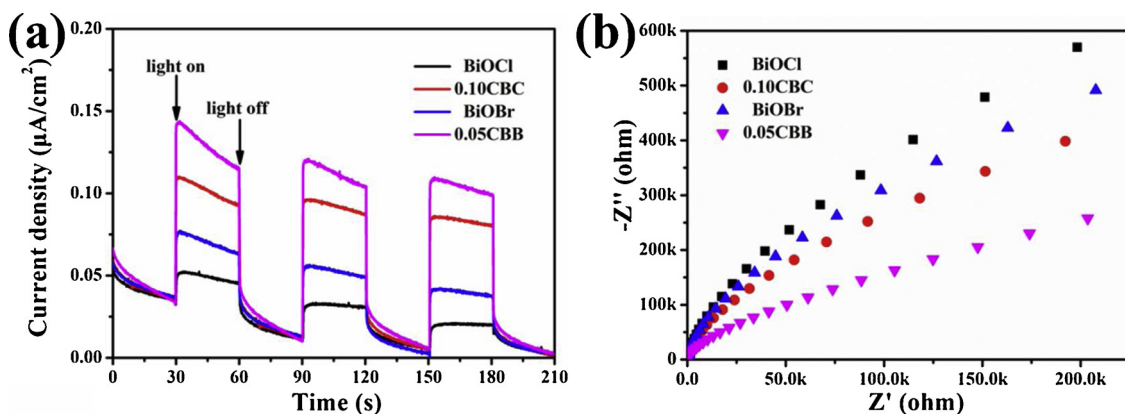


Fig. 13. (a) Plots of photocurrent density vs. irradiation time and (b) EIS spectra of BiOCl, BiOBr, 0.10CBC and 0.05CBB.

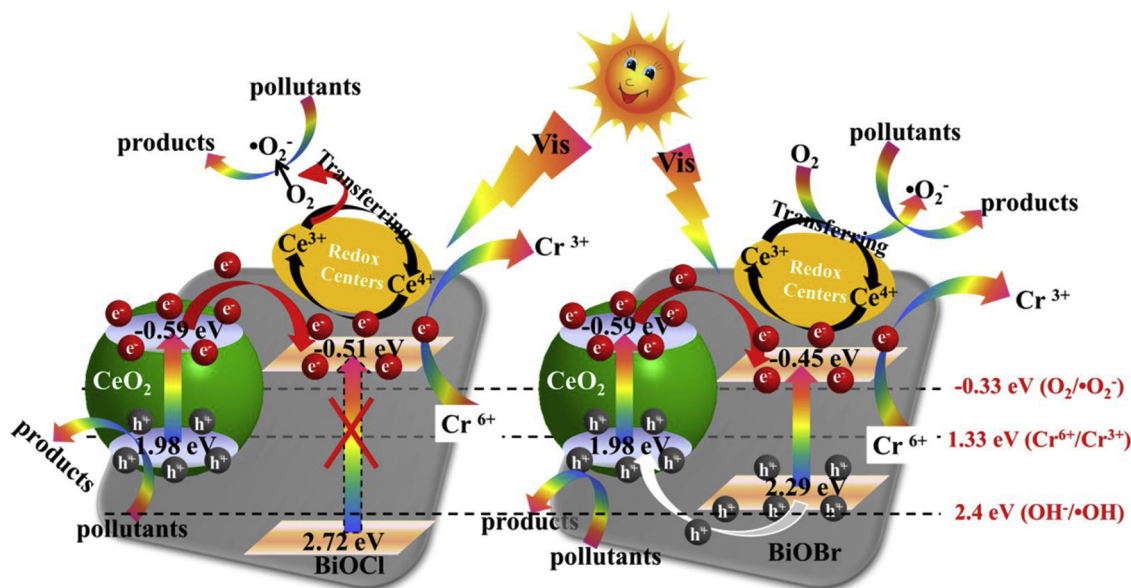
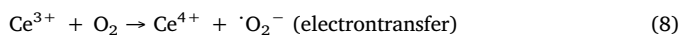


Fig. 14. A proposed schematic illustration showing the photocatalytic mechanism of CeO<sub>2</sub>/BiOCl and CeO<sub>2</sub>/BiOBr heterojunction photocatalysts.



This swift circulation system not only accelerated the transfer of electrons but also held up the recombination process of electrons and holes. Such effect of rare earth ions redox centers on boosting the photocatalyst activity has also been reported, such as La<sup>3+</sup>/La<sup>2+</sup> [55], Eu<sup>3+</sup>/Eu<sup>2+</sup> [56], Ce<sup>4+</sup>/Ce<sup>3+</sup> [35,54], Sm<sup>3+</sup>/Sm<sup>2+</sup> [57], Gd<sup>3+</sup>/Gd<sup>2+</sup> [58] etc. Especially, the CB potentials of BiOCl (-0.51 eV) and BiOBr (-0.45 eV) were more cathodic than that of O<sub>2</sub>/·O<sub>2</sub><sup>-</sup> (-0.33 eV), which exhibited a strong reductive ability [59]. As a result, the e<sup>-</sup> on the CB of the composites could reduce the absorbed O<sub>2</sub> on the surface of CeO<sub>2</sub> QDs/BiOX (X = Cl, Br) heterostructures to give birth to ·O<sub>2</sub><sup>-</sup>. On the other hand, the VB potential of CeO<sub>2</sub> (+1.98 eV) was not positive enough compared with the potential of ·OH/OH<sup>-</sup> (+2.4 eV) [43], suggesting most of h<sup>+</sup> were difficult to oxidize OH<sup>-</sup>/H<sub>2</sub>O to product ·OH radicals in the photocatalytic reaction. Accordingly, the h<sup>+</sup> was the dominating active species while the ·O<sub>2</sub><sup>-</sup> served as a secondary factor during the degradation process, which was consistent with the results of active species trapping experiments. Additionally, the CB positions of BiOCl and BiOBr were more negative than that of the standard reduction potential of Cr<sup>6+</sup>/Cr<sup>3+</sup> (+1.33 eV) [60], so the photocatalytic reduction of Cr<sup>6+</sup> was thermodynamically permissible. Understandably, it was reasonable to conclude that the fabrication of CeO<sub>2</sub> QDs/BiOX (X = Cl, Br) heterostructures with the Ce<sup>4+</sup>/Ce<sup>3+</sup> redox centers could achieve excellent photo-oxidation and reduction

ability.

#### 4. Conclusions

To summarize, we demonstrated a simple one-step low-temperature procedure for the controlled synthesis of CeO<sub>2</sub> QDs/BiOX (X = Cl, Br) heterojunctions with the inner Ce<sup>4+</sup>/Ce<sup>3+</sup> redox centers. It was found that the introduction of CeO<sub>2</sub> QDs could successfully narrow the band gap and boost visible light absorption, extending from UV light to visible light region. In particular, the CeO<sub>2</sub> QDs/BiOX (X = Cl, Br) heterojunction photocatalysts exhibited much higher photocatalytic performance than bare CeO<sub>2</sub>, BiOCl and BiOBr on the degradation of TC and reduction of Cr<sup>6+</sup> under 5 W white LED light irradiation. The immensely enhanced photocatalytic activity could be ascribed to fast separation efficiency and interfacial transference of photogenerated e<sup>-</sup>-h<sup>+</sup> pairs, which induced by the synergistic effects of inner Ce<sup>4+</sup>/Ce<sup>3+</sup> redox centers and the formation of intimately contacted interface between CeO<sub>2</sub> QDs and BiOX (X = Cl, Br). In comparison with the previously reported photocatalysts fabricated by tedious fabrication processes, the proposed procedure was relatively convenient, energy saving and environmental friendly, which was anticipated to be a highly promising strategy for the preparation of other photocatalytic materials.

## Acknowledgements

This work was supported by the National Natural Science Foundation of China (Grant Nos. 21571162), also partly supported by the JSPS KAKENHI Grant Number JP16H06439 (Grant-in-Aid for Scientific Research on Innovative Areas), the Dynamic Alliance for Open Innovation Bridging Human, Environment and Materials, the Cooperative Research Program of “Network Joint Research Center for Materials and Devices”.

## Appendix A. Supplementary data

Supplementary material related to this article can be found, in the online version, at doi:<https://doi.org/10.1016/j.apcatb.2019.03.017>.

## References

- J. Jiang, K. Zhao, X.Y. Xiao, L.Z. Zhang, Synthesis and facet-dependent photo-reactivity of BiOCl single-crystalline nanosheets, *J. Am. Chem. Soc.* 134 (2012) 4473–4476.
- F. Dong, T. Xiong, S. Yan, H.Q. Wang, Y.J. Sun, Y.X. Zhang, H.W. Huang, Z.B. Wu, Facets and defects cooperatively promote visible light plasmonic photocatalysis with Bi nanowires@BiOCl nanosheets, *J. Catal.* 344 (2016) 401–410.
- H.F. Cheng, B.B. Huang, Y. Dai, Engineering BiOX (X = Cl, Br, I) nanostructures for highly efficient photocatalytic applications, *Nanoscale* 6 (2014) 2009–2026.
- X.Y. Wu, K.K. Zhang, G.K. Zhang, S. Yin, Facile preparation of BiOX (X = Cl, Br, I) nanoparticles and up-conversion phosphors/BiOBr composites for efficient degradation of NO gas: Oxygen vacancy effect and near infrared light responsive mechanism, *Chem. Eng. J.* 325 (2017) 59–70.
- J.L. Hu, W.J. Fan, W.Q. Ye, C.J. Huang, X.Q. Qiu, Insights into the photosensitivity activity of BiOCl under visible light irradiation, *Appl. Catal. B Environ.* 158–159 (2014) 182–189.
- X.J. Wang, Q. Wang, F.T. Li, W.Y. Yang, Y. Zhao, Y.J. Hao, S.J. Liu, Novel BiOCl-C<sub>3</sub>N<sub>4</sub> heterojunction photocatalysts: in situ preparation via an ionic-liquid-assisted solvent-thermal route and their visible-light photocatalytic activities, *Chem. Eng. J.* 234 (2013) 361–371.
- X.J. Wang, W.Y. Yang, F.T. Li, J. Zhao, R.H. Liu, S.J. Liu, B. Li, Construction of amorphous TiO<sub>2</sub>/BiOBr heterojunctions via facets coupling for enhanced photocatalytic activity, *J. Hazard. Mater.* 292 (2015) 126–136.
- L. Ye, J. Liu, C. Gong, L. Tian, T. Peng, L. Zan, Two different roles of metallic Ag on Ag/AgX/BiOX (X = Cl, Br) visible light photocatalysts: surface plasmon resonance and Z-scheme bridge, *ACS Catal.* 2 (2012) 1677–1683.
- J. Tian, Y.H. Sang, Z.H. Zhao, W.J. Zhou, D.Z. Wang, X.L. Kang, H. Liu, J.Y. Wang, S.W. Chen, H.Q. Cai, H. Huang, Enhanced photocatalytic performances of CeO<sub>2</sub>/TiO<sub>2</sub> nanobelt heterostructures, *Small* 9 (2013) 3864–3872.
- Y. Zhao, T. Chen, R. Ma, J.F. Du, C. Xie, Synthesis of flower-like CeO<sub>2</sub>/BiOCl heterostructures with enhanced ultraviolet light photocatalytic activity, *Micro Nano Lett.* 13 (2018) 1394–1398.
- S. Zhang, D. Wang, Preparation of novel BiOBr/CeO<sub>2</sub> heterostructured photocatalysts and their enhanced photocatalytic activity, *RSC Adv.* 5 (2015) 93032–93040.
- X.J. Wen, C. Zhang, C.G. Niu, L. Zhang, G.M. Zeng, X.G. Zhang, Highly enhanced visible light photocatalytic activity of CeO<sub>2</sub> through fabricating a novel p-n junction BiOBr/CeO<sub>2</sub>, *Catal. Commun.* 90 (2017) 51–55.
- G.H. Carey, A.L. Abdelhady, Z. Ning, S.M. Thon, O.M. Bakr, E.H. Sargent, Colloidal quantum dot solar cells, *Chem. Rev.* 115 (2015) 12732–12763.
- M.Y. Ye, Z.H. Zhao, Z.F. Hu, L.Q. Liu, H.M. Ji, Z.R. Shen, T.Y. Ma, 0D/2D heterojunctions of vanadate quantum dots/graphitic carbon nitride nanosheets for enhanced visible-light-driven photocatalysis, *Angew. Chem. Int. Ed.* 56 (2017) 8407–8411.
- H. Imagawa, A. Suda, K. Yamamura, S. Sun, Monodisperse CeO<sub>2</sub> nanoparticles and their oxygen storage and release properties, *J. Phys. Chem. C* 115 (2011) 1740–1745.
- W. Chen, T.Y. Liu, T. Huang, X.H. Liu, J.W. Zhu, G.R. Duan, X.J. Yang, In situ fabrication of novel Z-scheme Bi<sub>2</sub>WO<sub>6</sub> quantum dots/g-C<sub>3</sub>N<sub>4</sub> ultrathin nanosheets heterostructures with improved photocatalytic activity, *Appl. Surf. Sci.* 355 (2015) 379–387.
- H.L. Wang, L.S. Zhang, Z.G. Chen, J.Q. Hu, S.J. Li, Z.H. Wang, J.S. Liu, X.C. Wang, Semiconductor heterojunction photocatalysts: design, construction, and photocatalytic performances, *Chem. Soc. Rev.* 43 (2014) 5234–5244.
- X.Y. Wu, J.T. Wang, G.K. Zhang, K. Katsumata, K. Yanagisawa, T. Sato, S. Yin, Series of M<sub>2</sub>WO<sub>3</sub>/ZnO (M = K, Rb, NH<sub>4</sub>) nanocomposites: combination of energy saving and environmental decontamination functions, *Appl. Catal. B Environ.* 201 (2017) 128–136.
- S.B. Yang, D.B. Xu, B.Y. Chen, B.F. Luo, X. Yan, L.S. Xiao, W.D. Shi, Synthesis and visible-light-driven photocatalytic activity of p-n heterojunction Ag<sub>2</sub>O/NaTaO<sub>3</sub> nanocubes, *Appl. Surf. Sci.* 383 (2016) 214–221.
- J.A. Seabold, K.S. Choi, Efficient and stable photo-oxidation of water by a bismuth vanadate photoanode coupled with an iron oxyhydroxide oxygen evolution catalyst, *J. Am. Chem. Soc.* 134 (2012) 2186–2192.
- Y.L. Tian, B.B. Chang, J.L. Lu, J. Fu, F.N. Xi, X.P. Dong, Hydrothermal synthesis of graphitic carbon nitride-Bi<sub>2</sub>WO<sub>6</sub> heterojunctions with enhanced visible light photocatalytic activities, *ACS Appl. Mater. Interfaces* 5 (2013) 7079–7085.
- Z. Wei, D. Benlin, Z. Fengxia, T. Xinyue, X. Jiming, Z. Lili, L. Shiyin, D.Y. Leung, C. Sun, A novel 3D plasmonic p-n heterojunction photocatalyst: Ag nanoparticles on flower-like p-Ag<sub>2</sub>S/n-BiVO<sub>4</sub> and its excellent photocatalytic reduction and oxidation activities, *Appl. Catal. B Environ.* 229 (2018) 171–180.
- X. Zhang, J. Zhang, J.Q. Yu, Y. Zhang, Z.X. Cui, Y. Sun, B.R. Hou, Fabrication of InVO<sub>4</sub>/AgVO<sub>3</sub> heterojunctions with enhanced photocatalytic antifouling efficiency under visible-light, *Appl. Catal. B Environ.* 220 (2018) 57–66.
- X.W. Zhang, L.C. Lei, Preparation of photocatalytic Fe<sub>2</sub>O<sub>3</sub>-TiO<sub>2</sub> coatings in one step by metal organic chemical vapor deposition, *Appl. Surf. Sci.* 254 (2008) 2406–2412.
- G.P. Zhang, D.Y. Chen, N.J. Li, Q.F. Xu, H. Li, J.H. He, J.M. Lu, Preparation of ZnIn<sub>2</sub>S<sub>4</sub> nanosheet-coated CdS nanorod heterostructures for efficient photocatalytic reduction of Cr (VI), *Appl. Catal. B Environ.* 232 (2018) 164–174.
- X.Y. Wu, X.Y. Wang, J. Li, G.K. Zhang, Boosting molecular oxygen activation of SrTiO<sub>3</sub> by engineering exposed facets for highly efficient photocatalytic oxidation, *J. Mater. Chem. A* 5 (2017) 23822–23830.
- J. Boltersdorf, L. Sullivan, T.L. Shelton, Z.K. Wu, M. Gray, B. Zoellner, F.E. Osterloh, P.A. Maggard, Flux synthesis, optical and photocatalytic properties of n-type Sn<sub>2</sub>TiO<sub>4</sub>: Hydrogen and oxygen evolution under visible light, *Chem. Mater.* 28 (2016) 8876–8889.
- K. Li, Y.J. Liang, J. Yang, Q. Gao, Y.L. Zhu, S.Q. Liu, R. Xu, X.Y. Wu, Controllable synthesis of {001} facet dependent four-square BiOCl nanosheets: A high efficiency photocatalyst for degradation of methyl orange, *J. Alloys Compd.* 695 (2017) 238–249.
- L. Chen, R. Huang, M. Xiong, Q. Yuan, J. He, J. Jia, M.Y. Yao, S.L. Luo, C.T. Au, S.F. Yin, Room-temperature synthesis of flower-like BiOX (X = Cl, Br, I) hierarchical structures and their visible-light photocatalytic activity, *Inorg. Chem.* 52 (2013) 11118–11125.
- W.Y. Lei, T.T. Zhang, L. Gu, P. Liu, José A. Rodríguez, G. Liu, M.H. Liu, Surface-Structure sensitivity of CeO<sub>2</sub> nanocrystals in photocatalysis and enhancing the reactivity with nanogold, *ACS Catal.* 5 (2015) 4385–4393.
- F. Dong, Q. Li, Y. Sun, W.K. Ho, Noble metal-like behavior of plasmonic Bi particles as a cocatalyst deposited on (BiO)<sub>2</sub>CO<sub>3</sub> microspheres for efficient visible light photocatalysis, *ACS Catal.* 4 (2014) 4341–4350.
- J.G. Wang, Y.J. Chen, W. Zhou, G.H. Tian, Y.T. Xiao, H.Y. Fu, H.G. Fu, Cubic quantum dot/hexagonal microsphere ZnIn<sub>2</sub>S<sub>4</sub> heterophase junctions for exceptional visible-light-driven photocatalytic H<sub>2</sub> evolution, *J. Mater. Chem. A Mater. Energy Sustain.* 5 (2017) 8451–8460.
- W.X. Zou, Y. Shao, Y. Pu, Y.D. Luo, J.F. Sun, K.L. Ma, C.J. Tang, F. Gao, L. Dong, Enhanced visible light photocatalytic hydrogen evolution via cubic CeO<sub>2</sub> hybridized g-C<sub>3</sub>N<sub>4</sub> composite, *Appl. Catal. B Environ.* 218 (2017) 51–59.
- S. Putla, M.H. Amin, B.M. Reddy, A. Nafady, K.A.A. Farhan, S.K. Bhargava, MnO<sub>x</sub> nanoparticle-dispersed CeO<sub>2</sub> nanocubes: a remarkable heteronanostructured system with unusual structural characteristics and superior catalytic performance, *ACS Appl. Mater. Interfaces* 7 (2015) 16525–16535.
- H.L. Jiang, M.L. Li, J. Liu, X.Q. Li, L. Tian, P.H. Chen, Alkali-free synthesis of a novel heterostructured CeO<sub>2</sub>-TiO<sub>2</sub> nanocomposite with high performance to reduce Cr (VI) under visible light, *Ceram. Int.* 44 (2018) 2709–2717.
- P. Zhang, Y. Liu, B. Tian, Y. Luo, J. Zhang, Synthesis of core-shell structured CdS@CeO<sub>2</sub> and CdS@TiO<sub>2</sub> composites and comparison of their photocatalytic activities for the selective oxidation of benzyl alcohol to benzaldehyde, *Catal. Today* 281 (2017) 181–188.
- X. Xiao, R. Hao, M. Liang, X.X. Zuo, J.M. Nan, L.S. Li, W.D. Zhang, One-pot solvothermal synthesis of three-dimensional (3D) BiOI/BiOCl composites with enhanced visible-light photocatalytic activities for the degradation of bisphenol-A, *J. Hazard. Mater.* 233–234 (2012) 122–130.
- F.T. Li, Q. Wang, J.R. Ran, Y.J. Hao, X.J. Wang, D.S. Zhao, S.Z. Qiao, Ionic liquid self-combustion synthesis of BiOBr/Bi<sub>2</sub>O<sub>3</sub>Br<sub>10</sub> heterojunctions with exceptional visible-light photocatalytic performances, *Nanoscale* 7 (2015) 1116–1126.
- N. Tian, H. Huang, C. Liu, F. Dong, T. Zhang, X. Du, S. Yu, Y. Zhang, In situ copolymerization fabrication of CeO<sub>2</sub>/g-C<sub>3</sub>N<sub>4</sub> n-n type heterojunction for synchronously promoting photo-induced oxidation and reduction properties, *J. Mater. Chem. A Mater. Energy Sustain.* 3 (2015) 17120–17129.
- D. Li, F.F. Shi, D.L. Jiang, M. Chen, W.D. Shi, CdIn<sub>2</sub>S<sub>4</sub>/g-C<sub>3</sub>N<sub>4</sub> heterojunction photocatalysts: enhanced photocatalytic performance and charge transfer mechanism, *RSC Adv.* 7 (2017) 231–237.
- X.J. Wen, C.G. Niu, L. Zhang, C. Liang, G.M. Zeng, A novel Ag<sub>2</sub>O/CeO<sub>2</sub> heterojunction photocatalysts for photocatalytic degradation of enrofloxacin: possible degradation pathways, mineralization activity and an in depth mechanism insight, *Appl. Catal. B Environ.* 221 (2018) 701–714.
- S. Iguchi, S. Kikkawa, K. Teramura, S. Hosokawa, T. Tanaka, Investigation of the electrochemical and photoelectrochemical properties of Ni-Al LDH photocatalysts, *Phys. Chem. Chem. Phys.* 18 (2016) 13811–13819.
- Y. Lin, S.H. Wu, X. Lia, X. Wu, C.P. Yang, G.M. Zeng, Y.R. Peng, Q. Zhou, L. Lu, Microstructure and performance of Z-scheme photocatalyst of silver phosphate modified by MWCNTs and Cr-doped SrTiO<sub>3</sub> for malachite green degradation, *Appl. Catal. B Environ.* 227 (2018) 557–570.
- J. Yang, Y.J. Liang, K. Li, Y.L. Zhu, S.Q. Liu, R. Xu, W. Zhou, Design of 3D flowerlike BiOCl<sub>2</sub>Br<sub>1-x</sub> nanostructure with high surface area for visible light photocatalytic activities, *J. Alloys Compd.* 725 (2017) 1144–1157.
- S.X. Ge, L.Z. Zhang, Efficient visible light driven photocatalytic removal of RhB and NO with low temperature synthesized In(OH)<sub>3</sub> hollow nanocubes: A comparative study, *Environ. Sci. Technol.* 45 (2011) 3027–3033.

- [46] P. Zhou, J.G. Yu, M. Jaroniec, All-Solid-State Z-Scheme Photocatalytic Systems, *Adv. Mater.* 26 (2014) 4920–4935.
- [47] J.B. Wang, D. Zhi, H. Zhou, X.W. He, D.Y. Zhang, Evaluating tetracycline degradation pathway and intermediate toxicity during the electrochemical oxidation over a Ti/Ti<sub>4</sub>O<sub>7</sub> anode, *Water Res.* 137 (2018) 324–334.
- [48] C. Wang, G.Z. Qu, T.C. Wang, F. Deng, D.L. Liang, Removal of tetracycline antibiotics from wastewater by pulsed corona discharge plasma coupled with natural soil particles, *Chem. Eng. J.* 346 (2018) 159–170.
- [49] Y. Liu, J.J. Kong, J.L. Yuan, W. Zhao, X. Zhu, C. Sun, J.M. Xie, Enhanced photocatalytic activity over flower-like sphere Ag/Ag<sub>2</sub>CO<sub>3</sub>/BiVO<sub>4</sub> plasmonic heterojunction photocatalyst for tetracycline degradation, *Chem. Eng. J.* 331 (2018) 242–254.
- [50] K. Qian, L. Xia, Z.F. Jiang, W. Wei, L.L. Chen, J.M. Xie, In situ chemical transformation synthesis of Bi<sub>4</sub>Ti<sub>3</sub>O<sub>12</sub>/I-BiOCl 2D/2D heterojunction systems for water pollution treatment and hydrogen production, *Catal. Sci. Technol.* 7 (2017) 3863–3875.
- [51] J. Ran, T.Y. Ma, G. Gao, X.W. Du, S.Z. Qiao, Porous P-doped graphitic carbon nitride nanosheets for synergistically enhanced visible-light photocatalytic H<sub>2</sub> production, *Energy Environ. Sci.* 8 (2015) 3708–3717.
- [52] L. Liang, F.C. Lei, S. Gao, Y.F. Sun, X.C. Jiao, J. Wu, S. Qamar, Y. Xie, Single unit cell bismuth tungstate layers realizing robust solar CO<sub>2</sub> reduction to methanol, *Angew. Chem. Int. Ed.* 54 (2015) 13971–13974.
- [53] H.L. Tan, X.M. Wen, R. Amal, Y.H. Ng, BiVO<sub>4</sub> {010} and {110} relative exposure extent: governing factor of surface charge population and photocatalytic activity, *J. Phys. Chem. Lett.* 7 (2016) 1400–1405.
- [54] M.L. Li, L.X. Zhang, M.Y. Wu, Y.Y. Du, X.Q. Fan, M. Wang, L.L. Zhang, Q.L. Kong, J.L. Shi, Mesoporous CeO<sub>2</sub>/g-C<sub>3</sub>N<sub>4</sub> nanocomposites: Remarkably enhanced photocatalytic activity for CO<sub>2</sub> reduction by mutual component activations, *Nano Energy* 19 (2016) 145–155.
- [55] J. Yang, Y.J. Liang, K. Li, G. Yang, Y.L. Zhu, S.Q. Liu, W. Lei, New reaction pathway induced by the synergistic effects of Bi plasmon and La<sup>3+</sup> doping for efficient visible light photocatalytic reaction on BiOCl, *Appl. Surf. Sci.* 458 (2018) 769–780.
- [56] N. Kaneva, A. Bojinova, K. Papazova, D. Dimitrov, Photocatalytic purification of dye contaminated sea water by lanthanide (La<sup>3+</sup>, Ce<sup>3+</sup>, Eu<sup>3+</sup>) modified ZnO, *Catal. Today* 252 (2015) 113–119.
- [57] F.Z. Wang, W.J. Li, S.N. Gu, H.D. Li, X. Wu, X.T. Liu, Samarium and nitrogen Co-Doped Bi<sub>2</sub>WO<sub>6</sub> photocatalysts: synergistic effect of Sm<sup>3+</sup>/Sm<sup>2+</sup> redox centers and N-doped level for enhancing visible-light photocatalytic activity, *Chem. Eur. J.* 22 (2016) 12859–12867.
- [58] X.C. Luo, G.Q. Zhu, J.H. Peng, X.M. Wei, M. Hojamberdiev, L. Jin, P. Liu, Enhanced photocatalytic activity of Gd-doped porous  $\beta$ -Bi<sub>2</sub>O<sub>3</sub> photocatalysts under visible light irradiation, *Appl. Surf. Sci.* 351 (2015) 260–269.
- [59] Z.H. Li, Z.P. Xie, Y.F. Zhang, L. Wu, X.X. Wang, X.Z. Fu, Wide band gap p-block metal oxyhydroxide InOOH: a new durable photocatalyst for benzene degradation, *J. Phys. Chem. C* 111 (2007) 18348–18352.
- [60] X.Y. Yuan, Q.Y. Jing, J.T. Chen, L. Li, Photocatalytic Cr(VI) reduction by mixed metal oxide derived from ZnAl layered double hydroxide, *Appl. Clay Sci.* 143 (2017) 168–174.